Stony Brook University

Event reconstruction and energy calibration using cosmic muons for the T2K pizero detector.

A Dissertation Presented

by

Le Trung

to

The Graduate School

in Partial Fulfillment of the

Requirements

for the Degree of

Doctor of Philosophy

in

Physics

Stony Brook University

December 2009

Stony Brook University

The Graduate School

Le Trung

We, the dissertation committee for the above candidate for the Doctor of Philosophy degree, hereby recommend acceptance of the dissertation.

Thesis advisor
Dr. Clark McGrew
Associate Professor of Physics

Chairperson of defense
Dr. Dmitri Tsybychev
Assistant Professor of Physics

Dr. George Sterman
Professor of Physics

Dr. Dmitri Donetski
Assistant Professor of Electrical Engineering

This dissertation is accepted by the Graduate School.

Lawrence Martin
Dean of the Graduate School

Abstract of the Dissertation

Event reconstruction and energy calibration using cosmic muons for the T2K pizero detector.

by

Le Trung

Doctor of Philosophy

in

Physics

Stony Brook University

2009

Neutrino oscillations were discovered in atmospheric and solar neutrinos and have been confirmed by experiments using neutrinos from accelerators and nuclear reactors. It has been found that there are large mixing angles in the $\nu_e \rightarrow \nu_\mu$ and $\nu_\mu \rightarrow \nu_\tau$ oscillations. The third mixing angle θ_{13}, which parameterizes the mixing between the first and the third generation, is constrained to be small by the CHOOZ reactor experiment. The T2K experiment is a long baseline neutrino oscillation experiment that uses the intense muon neutrino beam produced at J-PARC (Tokai, Japan) and Super-Kamiokande detector at 295 km as the far detector to measure the angle θ_{13} using the ν_e appearance channel. One dominant background to the ν_e appearance search is the single π^0 from neutral-current interactions. This background will be measured at the near site using the π^0 detector which was built at Stony Brook. The π^0 measurement requires a high rejection efficiency for backgrounds from charged-current neutrino interactions. We have

developed an event reconstruction specialized to reject the charged-current backgrounds while keeping the signal π^0. This event reconstruction was also used during the detector design phase to study its performance. Finally, we have done the energy calibration of the detector using cosmic ray muons.

To my family.

Contents

List of Figures

List of Tables

Acknowledgements

I would like to thank Clark for advising me and Chang Kee for financial support for many years. I appreciate help from other T2K members, I had a good time working in the collaboration. I also would like to thank professors Sterman, Tsybychev, and Donetski for being in the defense committee. Finally, I'm grateful to my family support.

Chapter 1

Introduction

Elementary particles are matter constituents that do not have any inner structure at currently accessible energies. The interactions among these matter constituents are carried out by interaction carriers. The matter constituents are categorized into *quarks* and *leptons*. Charged leptons are capable of electro-weak interactions while quarks further have strong interactions. Neutral leptons are named *neutrinos* and can only participate in weak interactions. There are three light active neutrinos, $(\nu_e, \nu_\mu, \nu_\tau)$, from the invisible width of Z decays[1], each with the flavor given by the accompanying charged lepton in weak decays. The interactions of elementary particles are completely determined by the Standard Model of particle physics. In the Standard Model, neutrinos are considered massless. However, recently there is strong evidence from neutrino oscillation experiments that neutrinos are massive and there are at least three distinct masses. This would require extension of the Standard Model. In the following, we will give a brief overview of neutrino physics which includes the measurements of the neutrino absolute mass scale, neutrinoless double beta decay, and neutrino oscillations.

1.1 Introduction to neutrino physics

There are many different experiments designed to measure different properties of neutrinos. Absolute value of neutrino masses can be measured directly from kinematic analysis of weak decays. Specifically, the most sensitive method for measuring the electron antineutrino mass is from studying the endpoint of the accompanying electron energy spectrum in tritium beta decay:

$$^3\mathrm{He} \rightarrow ^3\mathrm{He} + e^- + \bar{\nu}_e \tag{1.1}$$

The spectrum for zero neutrino mass ends in a straight line while in the case of $m_\nu \neq 0$ this spectrum has a horizontal component. There are various limits

reported by different groups[2, 3]. The best limit on electron antineutrino mass currently available ($m_{\nu_e} < 2.8\ eV/c^2$) has been reported by the Mainz group[4]. There is plan to measure this mass with one order of magnitude improvement of precision and sensitive to m_{ν_e} of 0.2 eV/c^2[5]. It should be mentioned that because of neutrino mixing, the electron antineutrino mass obtained above is actually an *effective* mass. It is the average of all mass eigenstates contributing to the neutrino. Their contributing fractions are given by the mixing matrix elements $|U_{ei}^2|$[6]

$$m_{\nu_e}^2 = \sum_i |U_{ei}^2| m_i^2. \tag{1.2}$$

The limit on the muon neutrino mass can be established from the kinematic analysis of the decay $\pi^+ \rightarrow \mu^+ + \mu_\nu$. The measurement of the muon momentum when the pion beam stops (or pion decays at rest) in the target allows to calculate the muon neutrino mass

$$m_{\nu_\mu}^2 = m_\pi^2 + m_\mu^2 - 2m_\pi \sqrt{m_\mu^2 + p_\mu^2} \tag{1.3}$$

The best estimate of the muon neutrino mass is $m_{\nu_\mu} < 160\ eV/c^2$[7].

Absolute values of neutrino masses can also be measured indirectly. An outstanding property of neutrinos still to be determined is if they are Majorana particles, i.e., not distinguishable from their antiparticles. This question can be answered by the so-called neutrinoless double beta decay ($0\nu 2\beta$). In a number of even-even nuclei, the beta decay is energetically forbidden while the double beta decay is energetically allowed. The double beta decays of these nuclei produce two electrons and two electron anti-neutrinos ($2\nu 2\beta$). However, if neutrinos are Majorana particles, then one neutrino emitted by one transition can be absorbed in the other transition. In this case, there are only two electrons and no neutrinos emitted from the decay ($0\nu 2\beta$). Therefore, this process also violates lepton number by two units. Because of neutrino mixing, all three neutrino mass eigenstates can contribute to $0\nu 2\beta$ decay. The decay is sensitive to the effective Majorana mass defined by[8]

$$m_{\beta\beta} = \left| \sum_i U_{ei}^2 m_i \right| = |c_{13}^2 c_{12}^2 m_1 + c_{13}^2 s_{12}^2 m_2 e^{i2\phi_2} + s_{13}^2 e^{i2\phi_3}| \tag{1.4}$$

This effective mass can be inferred from the measurement of the half-life of the double-beta process

$$[T_{1/2}^{0\nu 2\beta}]^{-1} = G_{0\nu} |\mathcal{M}_{0\nu}|^2 m_{\beta\beta}^2, \tag{1.5}$$

where $G_{0\nu}$ is the exactly calculable phase factor, $\mathcal{M}_{0\nu}$ the nuclear transition matrix element, and $m_{\beta\beta}$ the effective Majorana mass.

The experimental signature of $0\nu2\beta$ decay would be a peak in the spectrum of the energy deposited in the detector by the two electrons at the endpoint energy determined by the mass differences between the parent and daughter nuclei. On the other hand, the $2\nu2\beta$ decay has a continuous spectrum, extending to the endpoint energy. It should be emphasized that although the observation of $0\nu2\beta$ decay proves the Majorana mass nature of neutrinos, the measurement of the effective mass still requires better understanding of the nuclear matrix element.

Finally, most of the properties of the neutrino mass matrix can be measured in neutrino oscillation experiments. The concept of neutrino oscillation was first conceived by Pontecorvo[9]. It is the effect of neutrinos changing the their flavor as a result of propagation. The observation of neutrino oscillation would imply that neutrinos are massive. The oscillation is characterized the oscillation probability. A brief overview of neutrino masses, mixings, and expressions for oscillation probabilities are given in the next section. Extensive reviews on the theory of neutrino oscillations can be found in the literature. There are two ways to observe neutrino oscillations. In an *appearance* experiment, one creates a flux of neutrinos in association with charged leptons of one flavor and observes charged current reactions giving leptons of a different flavor. In a *disappearance* experiment, one creates a flux of neutrinos in association with charged leptons of one flavor and then measures a smaller flux in the inverse charged-current process.

1.2 Neutrino masses, mixings, and oscillations

In this section we will give an brief overview of the theory of neutrino masses, mixings, and oscillations. The neutrino masses and mixings will be discussed. Next we will derive the general probabilities for neutrino oscillation in vacuum and in a medium with constant density. Finally, we consider in more detailed the $\nu_\mu \to \nu_e$ appearance probability.

1.2.1 Neutrino masses and mixings

In relativistic field theory, there are two types of fermion mass term that are Lorentz invariant: Dirac mass and Majorana mass. The Dirac mass connects the left and right components of the same field while the Majorana mass connects the left and right components of conjugated fields. As a result, if neutrinos have Majorana mass, then they are their own anti-particles. In the standard electroweak theory, neutrinos are massless because of the limited particle content of the theory. There is no Dirac mass term since there are only left-handed neutrinos. There cannot be Majorana mass since the theory possesses a global symmetry corresponding to lepton number conservation. This symmetry forbids the Majorana mass term which violates the lepton number by $\Delta L = 2$. Therefore, any theory which can incorporate neutrino masses should be beyond the standard electroweak theory. It is well-known that it is not possible to distinguish between Dirac neutrinos and Majorana neutrinos in neutrino oscillation experiment in vacuum [10] and matter [11]. In this work, we will consider the oscillation of Dirac neutrinos. Introducing the right-handed component ν_R, we obtain the Dirac neutrino mass term of the form

$$\mathcal{L}_{mass} = \bar{\nu}_R M^0 \nu_L + h.c. = \bar{\nu}_{lR} M^0_{ll'} \nu_{l'L} + h.c., \quad l, l' = e, \mu, \tau, \tag{1.6}$$

where M^0 is a 3×3 complex matrix. In order to obtain physical states with definite masses, the mass matrix must be diagonalized. An arbitrary complex matrix can always be diagonalized by means of a bi-unitary transformation

$$V^+ M^0 U = m, \tag{1.7}$$

where V and U are unitary matrices and

$$m_{ik} = m_k \delta_{ik}. \tag{1.8}$$

Thus the mass term can be rewritten

$$\begin{aligned}\mathcal{L}_{mass} &= \sum_{i,k=1,2,3} \bar{\nu}_{iR}\delta_{ik}m_k\nu_{kL} + h.c. = \sum_{i=1,2,3} m_i\bar{\nu}_{iR}\nu_{iL} + h.c.\ , \\ &= \sum_{i=1,2,3} m_i\bar{\nu}_i\nu_i\ . \end{aligned} \tag{1.9}$$

Here

$$\nu_{lL} = \sum_{i=1,2,3} U_{li}\nu_{iL}, \quad l = e, \mu, \tau, \tag{1.10}$$

or equivalently,

$$\nu_f = U\nu \tag{1.11}$$

where $\nu_f = (\nu_e, \nu_\mu, \nu_\tau)$ is the flavor basis, and $\nu = (\nu_1, \nu_2, \nu_3)$ is the mass basis. From (1.9), we see that ν_i is a field of a neutrino with mass m_i. Equation (1.11) implies that the flavor fields ν_{lL} present in the standard electroweak lepton currents are linear combinations of the left-handed components of the fields of neutrinos with definite masses. The matrix U is called the neutrino mixing matrix.

The mixing matrix can be parameterized as follows. A general $n\times n$ unitary matrix has n^2 parameters. Among them $\frac{1}{2}n(n-2)$ parameters may be taken as Euler angles which is introduced in dealing with rotations in n dimensions. The remaining parameters are phases. However, $(2n-1)$ of these phases can be removed by rephasing the neutrino and charged lepton fields. Therefore, the number of phases in the mixing matrix is $\frac{1}{2}(n-1)(n-2)$. A 3×3 mixing matrix can have three mixing angles and one phase. The mixing matrix can be written as the product of three "rotation" matrices, where one of them has a phase :

$$U = U_{23}(\theta_{23})U_{13}(\theta_{13}, \delta)U_{12}(\theta_{12}), \tag{1.12}$$

where the angles are limited to the ranges $0 \le \theta_{ij} \le \frac{\pi}{2}$ and $0 \le \delta \le 2\pi$.

In practice, one usually employs the standard parameterization of the mixing matrix [12, 13]

$$\begin{aligned} U &= \begin{pmatrix} 1 & 0 & 0 \\ 0 & c_{23} & s_{23} \\ 0 & -s_{23} & c_{23} \end{pmatrix} \begin{pmatrix} c_{13} & 0 & s_{13}e^{-i\delta} \\ 0 & 1 & 0 \\ -s_{13}e^{i\delta} & 0 & c_{13} \end{pmatrix} \begin{pmatrix} c_{12} & s_{12} & 0 \\ -s_{12} & c_{12} & 0 \\ 0 & 0 & 1 \end{pmatrix} \\ &= \begin{pmatrix} c_{12}c_{13} & c_{13}s_{12} & e^{-i\delta}s_{13} \\ -s_{12}c_{23} - e^{i\delta}c_{12}s_{13}s_{23} & c_{12}c_{23} - e^{i\delta}s_{12}s_{13}s_{23} & c_{13}s_{23} \\ -e^{i\delta}c_{12}s_{13}c_{23} + s_{12}s_{23} & -e^{i\delta}s_{12}s_{13}c_{23} - c_{12}s_{23} & c_{13}c_{23} \end{pmatrix}, \end{aligned} \tag{1.13}$$

where we have denoted $\sin\theta_{ij} = s_{ij}$ and $\cos\theta_{ij} = c_{ij}$.

We have seen that the neutrino mass term causes neutrino mixing. The consequence of neutrino mixing is that weak eigenstates are combinations of mass eigenstates and the compositions are given by the mixing matrix elements. The mixing matrix can be parameterized by three angle angles and one phase. In the next section, we will show how neutrino mixing leads to neutrino oscillations.

1.2.2 Neutrino oscillations in vacuum and matter

It has been shown in the preceding section that neutrino mixing is a direct consequence of neutrino masses. In this section we will show how neutrino mixing can lead to neutrino oscillations. It should be emphasized that although any theory which accounts for neutrino masses should be beyond the standard electroweak theory, it is reasonable to assume that the production and detection of neutrinos are well described by the theory. Accordingly, neutrinos are produced in a specific flavor given by the accompanying lepton. The neutrino oscillations can be envisioned as follows. Because of neutrino mixing, a flavor neutrino state produced from weak decays is a linear combination of mass eigenstates with definite masses. In other words, the production of a neutrino with a given flavor is equivalent to the production of three neutrinos with different masses. During propagation, neutrino with different masses will develop different phases. These phase differences increase monotonically with time and travel distance. As a consequence, the probability of finding a neutrino of a given flavor is a periodic function of the distance between the source and the detector. This is called *neutrino oscillation*. In this section we will consider the quantum-mechanical treatment of neutrino oscillations. First we will derive the time evolution equation for neutrinos in vacuum, such an equation completely determines the vacuum propagation of neutrinos. Then we derive the general expressions for oscillation probabilities.

Consider a system of three neutrinos $\nu = (\nu_1, \nu_2, \nu_3)$ with definite masses having the same momentum p. Let $\psi = (\psi_1, \psi_2, \psi_3)$ be the corresponding wave functions. The time evolution of ψ is determined by the Schrodinger-like equation:

$$i\frac{d\psi}{dt} = H_0\psi, \tag{1.14}$$

where for free propagation of neutrinos in vacuum we have

$$H_0\psi_i = E_i\psi_i, \quad E_i = \sqrt{p^2 + m_i^2}. \tag{1.15}$$

We limit ourselves to the ultra-relativistic limit, i.e. $p \gg m_i$, then we can approximate

$$E_i \simeq p + \frac{m_i^2}{2p} \simeq p + \frac{m_i^2}{2E}. \tag{1.16}$$

It should be emphasized that the appearance of the term proportional to the unit matrix in the Hamiltonian in the right hand side of (1.14) is equivalent to changing all neutrino fields by the same phase factor; it leads to no physical consequences. Therefore, we can always omit such a term in the Hamiltonian. The time evolution equation becomes:

$$i\frac{d\psi}{dt} = \frac{1}{2E}\begin{pmatrix} m_1^2 & 0 & 0 \\ 0 & m_2^2 & 0 \\ 0 & 0 & m_3^2 \end{pmatrix}\psi. \tag{1.17}$$

This equation completely determines the vacuum propagation of neutrinos. Next we are going to find the oscillation probabilities. Let us consider a neutrino state of a given flavor produced in weak interaction with momentum p. Such a flavor state is a superposition of states with definite masses:

$$\mid \nu_l >= \sum_{i=1,2,3} U_{li} \mid \nu_i > . \tag{1.18}$$

During propagation, different neutrino components will develop different phases. This difference in phases increases monotonically with time. The flavor state at the time t after production is

$$\mid \nu_l(t) >= \sum_{i=1,2,3} U_{li} e^{-i\frac{m_i^2}{2E}t} \mid \nu_i > . \tag{1.19}$$

Due to the unitarity of the mixing matrix, we can invert (1.18) and express the mass eigenstates in terms of flavor states

$$\mid \nu_i >= \sum_{l'=e,\mu,\tau} U^*_{l'i} \mid \nu_{l'} >, \tag{1.20}$$

then

$$\mid \nu_l(t) >= \sum_{i,l'} U_{li} U^*_{l'i} e^{-i\frac{m_i^2}{2E}t} \mid \nu_{l'} > . \tag{1.21}$$

The oscillation amplitude from a neutrino of flavor l to a neutrino of flavor l', $A(\nu_l \to \nu_{l'})$, at the time t after production is

$$A(\nu_l \to \nu_{l'}) \equiv < \nu_{l'} \mid \nu_l(t) >= \sum_i U_{li} U^*_{l'i} e^{-i\frac{m_i^2}{2E}t}. \tag{1.22}$$

Consequently, the oscillation probability equals

$$P(\nu_l \to \nu_{l'}) \equiv \mid A(\nu_l \to \nu_{l'}) \mid^2 = \sum_{i,j} U_{li} U^*_{lj} U^*_{l'i} U_{l'j} e^{-i\frac{m_i^2 - m_j^2}{2E}L}, \tag{1.23}$$

where in the ultra-relativistic limit ($c \simeq 1$) $L \simeq t$ and L is the distance from the source. Let us define the oscillation phase as

$$\varphi_{ij} \equiv \frac{m_i^2 - m_j^2}{4E} L. \tag{1.24}$$

It is noted that the oscillation phase depends on the ratio L/E_ν, which we will see later, characterizes neutrino oscillation experiments. Then we can write the oscillation probability

$$\begin{aligned} P(\nu_l \to \nu_{l'}) &= \sum_{i,j} U_{li} U^*_{lj} U^*_{l'i} U_{l'j} e^{-2i\varphi_{ij}} \\ &= \sum_{i,j} U_{li} U^*_{lj} U^*_{l'i} U_{l'j} (e^{-2i\varphi_{ij}} - 1 + 1) \\ &= \delta_{ll'} - \sum_{i \neq j} U_{li} U^*_{lj} U^*_{l'i} U_{l'j} (e^{-2i\varphi_{ij}} - 1). \end{aligned} \tag{1.25}$$

Defining the quantity $J^{ll'}_{ij} = U_{li} U^*_{lj} U^*_{l'i} U_{l'j}$, and writing $J^{ll'}_{ij} = \mathrm{Re} J^{ll'}_{ij} + i \mathrm{Im} J^{ll'}_{ij}$, one can show that

$$J^{ll'}_{ij} (e^{-2i\varphi_{ij}} - 1) = -2\mathrm{Re} J^{ll'}_{ij} \sin^2 \varphi_{ij} + \mathrm{Im} J^{ll'}_{ij} \sin 2\varphi_{ij}. \tag{1.26}$$

Finally, substituting $J^{ll'}_{ij}$ into (1.25) and using (1.26) we obtain the well-known formula for the neutrino oscillation probabilities

$$P(\nu_l \to \nu_{l'}) = \delta_{ll'} - 4 \sum_{i>j} \mathrm{Re} J^{ll'}_{ij} \sin^2 \varphi_{ij} + 2 \sum_{i>j} \mathrm{Im} J^{ll'}_{ij} \sin 2\varphi_{ij}. \tag{1.27}$$

Some properties of the oscillation probabilities can be obtained immediately from (1.27):

- Using the unitarity of the mixing matrix, we find from (1.23) that the total probability of oscillation of a given flavor into neutrinos of all flavors is unity.

- If all neutrinos are degenerate in masses then $P(\nu_l \to \nu_{l'}) = \delta_{ll'}$, that is no neutrino oscillations.

- If there were no mixing, i.e. $U_{li} = \delta_{li}$, then we would also have $P(\nu_l \to \nu_{l'}) = \delta_{ll'}$.
- The first sum is CP even, and the second sum is CP odd.

Remember that we mentioned that neutrino oscillation experiments can not distinguish between Majorana and Dirac neutrinos. This is because Majorana neutrino mixing involves two extra phases, $U \to U diag(1, e^{i\phi_2}, e^{i\phi_3})$. These Majorana phases cancel out in the oscillation probabilities, and thus cannot be probed via neutrino oscillations.

Neutrino oscillations in matter

As a beam of neutrinos traverse a medium, neutrinos can interact with electrons in the medium. Neutrinos also interact with nucleons, but the cross section is much smaller than with electrons. However, electron neutrino interacts differently with electrons compared with the other two neutrinos. Specifically, electron neutrino can interact by exchanging either a W or Z boson while muon neutrino and tau neutrino can interact only by exchanging Z. The interaction of all three neutrinos by exchanging the Z boson gives rise to a potential energy term in the Hamiltonian. This potential energy term is the same for all three neutrino flavors and thus can be absorbed into a global phase of the neutrino fields. However, the potential energy term of electron neutrino because of exchanging the W boson cannot be absorbed and hence has physical consequences. This is called MSW effect[14].

Let us consider the oscillation of three neutrino flavors in matter with constant density profile. The time evolution equation for neutrino flavor states ψ_f in matter is given by

$$i\frac{d\psi_f}{dt} = \mathcal{H}\psi_f, \tag{1.28}$$

the effective Hamiltonian is

$$\mathcal{H} = \frac{1}{2E_\nu}\left[U\begin{pmatrix} m_1^2 & 0 & 0 \\ 0 & m_2^2 & 0 \\ 0 & 0 & m_3^2 \end{pmatrix}U^\dagger + \begin{pmatrix} A & 0 & 0 \\ 0 & 0 & 0 \\ 0 & 0 & 0 \end{pmatrix}\right] . \tag{1.29}$$

Here $U = U_{23}(\theta_{23})U_{13}(\theta_{13}, \delta)U_{12}(\theta_{12})$ is the mixing matrix (1.13), which rotates from mass basis to flavor basis. The second term arises from the weak charged current interactions of ν_e with electrons in matter $A = 2VE_\nu$ and $V = \sqrt{2}G_F n_e$, where G_F is the Fermi coupling constant and n_e is the electron density of the medium traversed by the neutrino beam. It is noted that the matter potential is monotonically increases with electron density and neutrino

energy. The oscillation probabilities in matter can be obtained similarly to the oscillation probabilities in vacuum:

$$P^m(\nu_l \to \nu_{l'}) = \delta_{ll'} - 4\sum_{i>j} \mathrm{Re}\mathcal{J}_{ij}^{ll'} \sin^2 \varphi_{ij}^m + 2\sum_{i>j} \mathrm{Im}\mathcal{J}_{ij}^{ll'} \sin 2\varphi_{ij}^m, \qquad (1.30)$$

where we have defined

$$\mathcal{J}_{ij}^{ll'} = U_{li}^m U_{lj}^{m*} U_{l'i}^{m*} U_{l'j}^m, \qquad (1.31)$$

$$\varphi_{ij}^m = \Delta \frac{\lambda_i - \lambda_j}{4E_\nu} L. \qquad (1.32)$$

Here U^m is the mixing matrix in matter, λ_i are effective neutrino masses in matter, and $\Delta = \Delta m_{31}^2$. The mixing matrix in matter can be parameterized similar to that in vacuum. The relationship between the mixing angles in vacuum and the mixing angles in matter is given in [15]. It is emphasized that since the Earth medium is CP asymmetric, there is CP violation effect arising from the neutrino propagation in addition to the intrinsic CP violation effects from the complex phase in the mixing matrix.

1.2.3 The $(\nu_\mu \to \nu_e)$ appearance channel

Of the oscillation channels whose oscillation probabilities given by (1.27), the $\nu_\mu \to \nu_e$ appearance channel is of particular interest. First a nearly pure beam of (anti-)muon neutrinos can be produced from accelerator. Second as we will see in the following. The full $\nu_\mu \to \nu_e$ oscillation probability is a complicated function of the mixing angles. However, the oscillation probability could be expanded in terms of the small mass hierarchy parameter $\alpha \equiv \Delta m_{21}^2 / \Delta m_{31}^2$. Neglecting the matter effects, which is a good approximation for the T2K low energy beam and short baseline, and the CP violation terms, the $\nu_\mu \to \nu_e$ oscillation probability can be written as[16]

$$P(\nu_\mu \to \nu_e) \approx \sin^2\theta_{23} \sin^2 2\theta_{13} \sin^2 \frac{\Delta m_{32}^2 L}{4E_\nu} \qquad (1.33)$$

where we have kept only the zero-order term of α. It is noticed that the oscillation amplitude is proportional to the $\sin^2 2\theta_{13}$. Measurement of this oscillation channel will give a direct measurement of the mixing angle θ_{13}. The oscillation amplitude is also proportional to the atmospheric neutrino mixing angle θ_{23}. In addition, the phase of the oscillation depends on the atmospheric neutrino mass squared difference, Δm_{32}^2. Therefore, to measure the mixing angle θ_{13}, it is necessary to make precise measurements of the atmospheric

neutrino oscillation parameters, $(\sin^2 2\theta_{23}, \Delta m^2_{32})$. Since the oscillation phase is proportional to the ratio L/E_ν, for an experiment of a given baseline and narrow-band neutrino beam, the peak energy is chosen so as to maximize the oscillation probability. The probability (1.33) is plotted as a function of the neutrino energy E_ν for the T2K baseline (295 km) in Fig. 1.1. The first oscillation maximum is around the neutrino energy of 0.7 GeV. The following parameters are used to make the plot. The angle θ_{13} is about the CHOOZ limit, $\sin^2 2\theta_{13} = 0.15$ and $(\sin^2 2\theta_{23} = 1.0,\ \Delta m^2_{32} = 2.5 \times 10^{-3}\ \mathrm{eV}^2)$

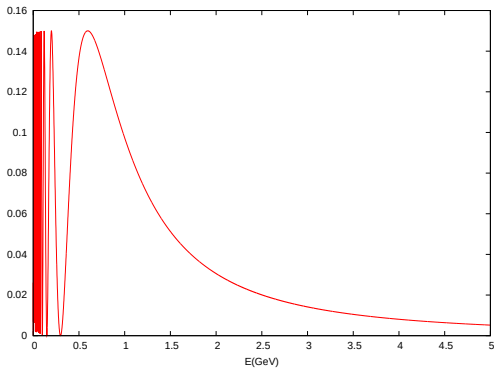

Figure 1.1: The $\nu_\mu \rightarrow \nu_e$ oscillation probability as a function of the neutrino energy E_ν for the T2K baseline (295 km). The angle θ_{13} is about the CHOOZ limit, $\sin^2 2\theta_{13} = 0.15$ and the atmospheric oscillation parameters are $(\sin^2 2\theta_{23} = 1.0,\ \Delta m^2_{32} = 2.5 \times 10^{-3}\ \mathrm{eV}^2)$.

1.3 Overview of neutrino oscillation experiments

Neutrino oscillations have been discovered in atmospheric[17] and solar neutrinos[18, 19]. They were confirmed by experiments using neutrinos produced by accelerators[20, 21] and reactors[22]. Two mixing angles have been measured and they are found much larger than the mixing angles in the quark sector. Atmospheric and accelerator neutrino oscillation experiments measure the mixing angle θ_{23} which parameterizes the mixing of the second and the third lepton generation and the corresponding squared mass difference, Δm^2_{23}. Solar and reactor (with baseline around 100 km) neutrino oscillation experiments measure the mixing angle θ_{12} between the first and second generation. The correct sign of Δm^2_{21} was established thanks to the matter effects in solar neutrino oscillation. The neutrino oscillation results require that neutrinos

have masses and there are at least three distinct masses. However, the neutrino oscillation between the first and the third generation has not been found. Currently there is a limit on the mixing angle θ_{13} from the CHOOZ reactor experiment[23]. It is interesting to see if this mixing angle is nonzero. If the last mixing angle is found to be different from zero, then similar to the quark sector, the complex phase in the mixing matrix could generate CP violation in the lepton sector. In this section, we will give a short review of neutrino oscillation experiments and the current values of the oscillation parameters.

1.3.1 Solar neutrino experiments

Electron neutrinos are produced from the fusion reactions at the core of the Sun. The fuel burning mechanism is described by standard solar model[24]. The energy spectrum of solar neutrinos for the solar model is shown in Fig. 1.2. The first experiment to detect neutrinos from the Sun is the Homestake experiment which used the radiochemical method. The experiment detects neutrinos by the reaction $^{37}\mathrm{Cl}(e,\nu_e)^{37}\mathrm{Ar}$ (for $E_\nu > 0.814$ MeV) suggested by Pontecorvo and Alvarez. It is sensitive to the high energy of the ^8B component of the solar neutrino spectrum. Neutrinos react with Cl in the detector and produce Ar, which has a half-life of 35 days. The produced Ar is then extracted and purified. The purified Ar decays are counted by loading the purified Ar into a proportional chamber filled with methane as counting gas. The efficiency of the detector was about 25 Ar atoms per year. The result of the experiment found that the number of B neutrinos is substantially lower than that predicted by the standard solar model.

Two other radiochemical neutrino experiments which use gallium are sensitive to low energy neutrinos from pp reactions[25, 26]. This is because the nuclear reaction $^{71}\mathrm{Ga}(e,\nu_e)^{71}\mathrm{Ge}$ has a low threshold of 233 keV. Both experiments found the solar neutrino flux lower than the standard solar model predictions.

The Kamiokande (and later Super-Kamiokande) experiments used a huge water tank to detect solar neutrinos. These experiments detect neutrinos by the Cherenkov light from the recoiled electron from neutrino elastic scattering

$$\nu_x + e^- \rightarrow \nu_x + e^- \tag{1.34}$$

The light is detected by photomultipliers (PMTs) which view the inside of the detector. The direction of the electron is reconstructed using the position of the PMTs and recorded light intensities. These experiments can detect neutrinos in real time. The fact that electron angular distribution peaks around the

incident neutrinos help remove isotropic background. The result from the Super-Kamiokande effective 1496 days of running is

$$\phi_{\nu_e}(^8B) = 2.35 \pm 0.02 \pm 0.08 \times 10^6/cm^2 sec. \tag{1.35}$$

This is about 46% of the standard solar neutrino flux prediction.

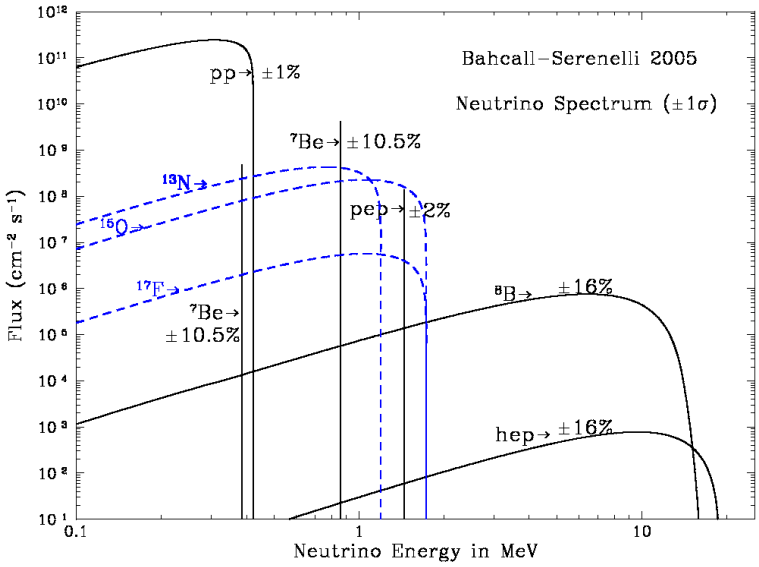

Figure 1.2: Solar neutrino energy spectrum for the solar model.

The Davis Cl experiment, SAGE[25], GALLEX[26] (later GNO)[27], Kamiokande, and the high-statistics Super-Kamiokande electron neutrino scattering measurements produced results that were incompatible with either standard or nonstandard solar model predictions [28, 29]. However, the results accord with the hypothesis of neutrino oscillations in the (ν_1, ν_2) sector which is governed by the mass-mixing parameters $(\Delta m^2_{21}, \theta_{12})$. For a long time the hypothesis admitted a multiplicity of possible solutions resulting from either the vacuum or MSW oscillations and spanning several orders of magnitude in both mass and mixing parameters. A clear preference for MSW solutions at large mixing angle only emerged with high-statistics Super-Kamiokande data[18].

A direct proof that solar ν_e underwent a flavor change (affected by solar matter) came only recently with the Sudbury Neutrino Observatory (SNO) experiment, a heavy water Cherenkov detector[19]. The heavy water target

provided three different reactions for ^{8}B

$$\nu_e + d \rightarrow p + p + e^- \qquad \text{(CC)} \tag{1.36}$$
$$\nu_\alpha + d \rightarrow n + p + \nu_\alpha \qquad \text{(NC)} \tag{1.37}$$
$$\nu_\alpha + e^- \rightarrow \nu_\alpha + e^- \qquad \text{(ES)} \tag{1.38}$$

The charged current (CC) reaction is only sensitive to electron neutrinos whereas the neutral current (NC) reaction is sensitive to all active neutrino flavors. The measurement of the neutrino flux using neutral current interaction (NC) will provide a check for the standard solar model prediction of the total ^{8}B flux independent of neutrino oscillations. The elastic scattering (ES) reaction is also sensitive to all flavors, but with reduced sensitivity ν_μ and ν_τ. The electrons from the neutrino reactions are detected by Cherenkov light. The protons have momentum far below the Cherenkov threshold, and hence are not detected. The neutron from neutral-current reaction is detected by the neutron capture process. In the second stage of the experiment, salt was added to increase the sensitivity to this reaction, adding the neutron capture on ^{35}Cl in addition to the capture on deuterium.

The combination of the KamLAND and the global fit of solar neutrinos gives the best-fit values for the solar neutrino oscillation parameters, ($\theta_{12} \sim 37^0, \Delta m^2_{21} \sim 7.6 \times 10^{-5}$ eV^2) (Fig. 1.3).

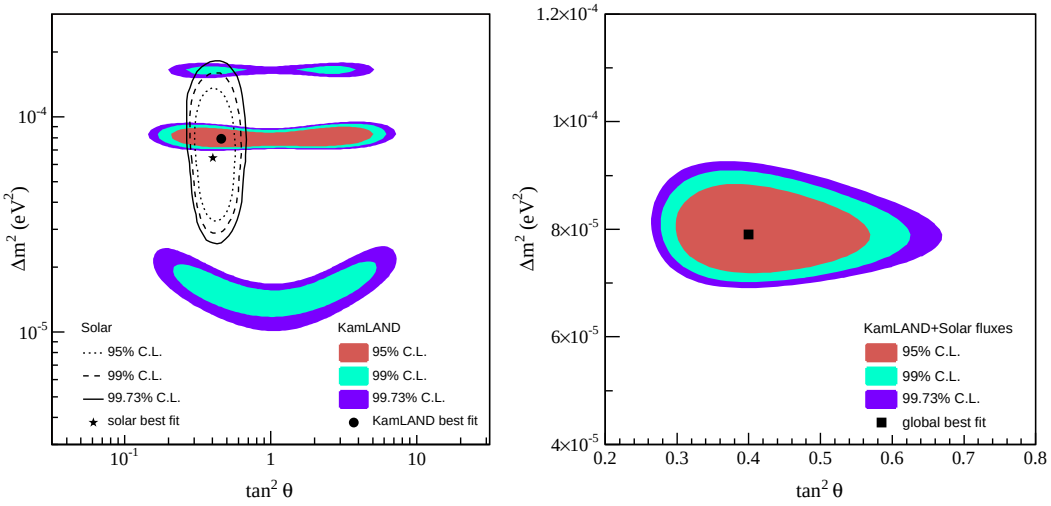

Figure 1.3: Combination of the KamLAND and the global fit of KamLAND and solar fluxes (2 neutrino oscillation analysis).

1.3.2 Atmospheric neutrino oscillation experiments

Atmospheric neutrinos are produced by the interaction of cosmic rays with nuclei in the upper atmosphere through the decay chain, $\pi, K \rightarrow \mu \rightarrow e$. The decay chain creates approximately two $\nu_\mu + \bar{\nu}_\mu$ for every $\nu_e + \bar{\nu}_e$. Because of the isotropy of the cosmic rays and the spherical atmosphere, it is expected that the atmospheric neutrino flux is up-down symmetric with respect to the zenith angle. The Super-Kamiokande collaboration which uses a large (50 kton) water Cherenkov detector can reconstruct the direction and hence the path length L of the ν from the atmosphere. The path length ranges from $L \sim 15$ km for downgoing neutrinos to $L \sim 13{,}000$ km for upgoing neutrinos. The data showed a clear up-down angular asymmetry of atmospheric ν_μ flux with less ν_μ from the longest path length L. On the other hand, there is no up-down asymmetry in the ν_e flux[17]. Therefore, the zenith angle distribution of atmospheric neutrinos can be interpreted as arising from the $\nu_\mu \rightarrow \nu_\tau$ flavor change. An analysis of the Super-Kamiokande data which used only events with good resolution of L/E showed an oscillatory signature in atmospheric neutrino oscillations[30, 31]. The ratio of the data to the MC events without neutrino oscillation as a function of the reconstructed L/E is shown in Fig. 1.4. The solid line is the best-fit, $(\sin^2 2\theta, \Delta m^2) = (1.00, 2.4 \times 10^{-3}\ \mathrm{eV}^2)$, expectation for two flavor $\nu_\mu \rightarrow \nu_\tau$ oscillation. A dip, which should correspond to the first oscillation maximum, is observed around $L/E = 500$ km/GeV. This rules out other hypotheses such as neutrino decay which could explain the deficit in the ν_μ flux.

1.3.3 Accelerator-based neutrino oscillation experiments

Neutrino oscillations can be probed by using neutrinos produced by accelerators. In these experiments, the proton beam from an accelerator hits a target to produce pions. A magnetic horn system is used to select pions of desired charge and focus the pion beam. The pions in turn decay in a tunnel into muons and neutrinos, mostly in the forward direction. A beam dump is placed at the end of the decay tunnel to stop all particles but the neutrinos. The neutrino flux and spectrum are measured at two sites, usually at a near site and far site. The neutrino spectrum and the baseline are dictated by the oscillation parameter Δm^2 that the experiment plans to probe. The flux and spectrum at the near and far site are then compared to search for neutrino oscillations. The accelerator neutrino experiments can be sensitive to both atmospheric oscillation through disappearance measurement and θ_{13} through $\nu_\mu \rightarrow \nu_e$ appearance. It should be noted that high statistics measurements of

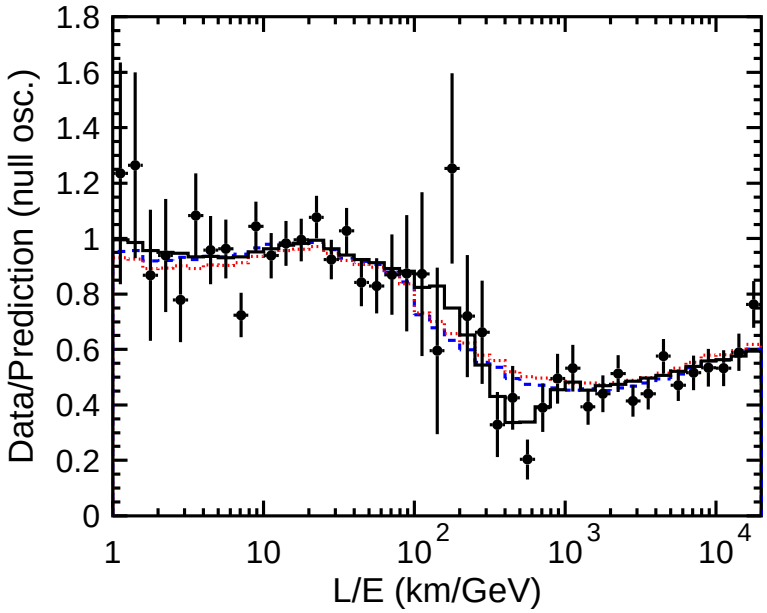

Figure 1.4: Ratio of the data to the MC events without neutrino oscillation (points) as a function of the reconstructed L/E together with the best-fit expectation for 2-flavor $\nu_\mu \to \nu_\tau$ oscillation (solid line). Error bars are statistical only. The best-fit expectation for neutrino decay (dashed line) and neutrino decoherence (dotted line) are also shown[30].

various neutrino cross sections can also be carried out at the near site using the high intensity neutrino flux.

The K2K is the first accelerator-based neutrino experiment, designed to confirm the oscillation of atmospheric neutrinos. The experiment uses the 12 GeV proton beam at KEK to produce neutrinos of 1.4 GeV mean energy and the Super-Kamiokande as the far detector 250 km away. The experiment found the spectrum suppression and distortion at the far site. The allowed region of Δm^2 and $\sin^2\theta_{23}$ is consistent with atmospheric neutrino oscillations.

The MINOS experiment uses the NuMI beam line at Fermilab and a far detector 735 km away to measure the oscillation of ν_μ ($\bar{\nu}_\mu$). The results based on 3.36×10^{20} POT from the NuMI beam are $|\Delta m^2| = (2.43 \pm 0.13) \times 10^{-3}$ eV^2 (68% C.L.) and the mixing angle $\sin^2 2\theta > 0.90$ (90% C.L)[32].

1.3.4 Reactor-based neutrino oscillation experiments

In addition to accelerator-based neutrino experiments where a beam of ν_μ ($\bar{\nu}_\mu$) is usually used, there are also reactor-based neutrino experiments.

This type of neutrino oscillation experiment uses intense $\bar{\nu}_e$ flux produced by nuclear fission reactions in nuclear reactors. Since $\bar{\nu}_e$ neutrinos from reactors are low energy ($E_\nu \sim 5$ MeV), below μ, τ production threshold, reactor-based experiments are of disappearance type experiment in which one measures the survival probability of neutrinos. The survival probability in the case of three-flavor neutrinos can be approximately written as

$$\mathrm{P}(\bar{\nu_e} \to \bar{\nu_e}) \approx 1 - \sin^2\theta_{13}\sin^2\frac{\Delta m^2_{32}}{4E_\nu}L - \cos^4\theta_{13}\sin^2\theta_{12}\sin^2\frac{\Delta m^2_{21}}{4E_\nu}L \quad (1.39)$$

It is seen from (1.39) that the oscillation probability has two distinctive terms: the atmospheric and solar oscillation terms. Depending on the baseline, reactor-based experiment can be sensitive to either atmospheric or solar neutrino oscillation parameters. Remarkably, the atmospheric oscillation term which corresponds to the short baseline (a few km) has the oscillation amplitude proportional to the unknown mixing angle θ_{13}. Therefore, reactor-based experiment with short baseline is an excellent way to measure θ_{13}. The $\bar{\nu}_e$ are detected using the inverse beta decay

$$\bar{\nu}_e + p \to e^+ + n. \quad (1.40)$$

The experimental signature in a detector is a prompt positron annihilation with a pair of back-to-back γs of 0.511 MeV energy, followed by a neutron capture producing a delayed signal.

Palo Verde and CHOOZ reactor neutrino experiments The Palo Verde experiment is located in Phoenix, Arizona. It studies the oscillation of $\bar{\nu}_e$ from the Palo Verde nuclear power plants about 1 km away[33]. The short baseline makes the detector sensitive to $\Delta m^2_{31} \sim 10^{-3}$ eV^2. The experiment has no near detector, and hence the flux and energy spectrum of unoscillated $\bar{\nu}_e$ are calculated from the reactor power and fuel composition. It was found that the ratio of the observed interaction rate to the one expected for no oscillations is $R_{\mathrm{obs}}/R_{\mathrm{calc}} = 1.01 \pm 0.024(\mathrm{stat}) \pm 0.053(\mathrm{sys})$. Most of the uncertainties in the experimental results come from the systematic uncertainties in the neutrino flux and detection efficiency[34].

Currently, the most stringent limit on the mixing angle θ_{13} came from the results of the CHOOZ reactor experiment[23]. The CHOOZ experiment has similar baseline to the Palo Verde experiment, the detector is located about 1 km from CHOOZ nuclear power plant, France. The final result was also given as the ratio of the number of measured events to the number of expected events for no oscillations, averaged on energy spectrum

$$R = 1.02 \pm 2.8\%(\mathrm{stat}) \pm 2.7\%(\mathrm{sys}). \quad (1.41)$$

It was found that there was no evidence of $\bar{\nu}_e$ disappearance at 90% CL for the parameter region given approximately by $\Delta m^2 > 7 \times 10^{-4}$ eV^2 at maximum mixing and $\sin^2 2\theta = 0.1$ at large Δm^2. In Fig. 1.5 we show the region in the $\Delta m^2_{32} - \sin^2\theta_{13}$ plane excluded by the CHOOZ experiment. The corresponding limit on θ_{13} is $\sin^2\theta_{13} > 0.17$ for large Δm^2[35].

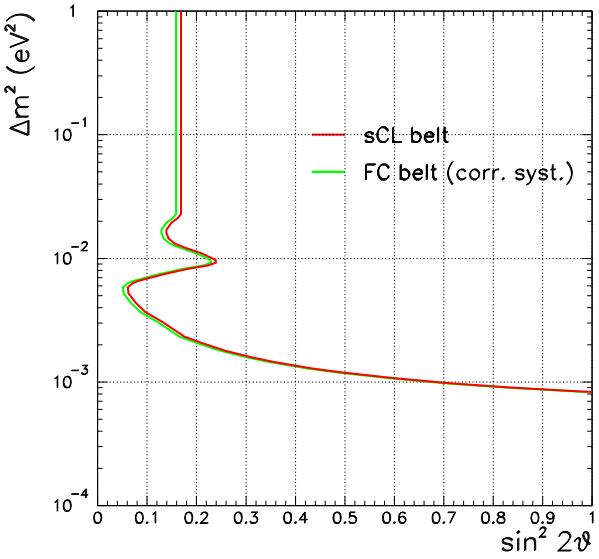

Figure 1.5: Exclusion plot at 90% CL for the oscillation parameters based on the differential energy spectrum.

KamLAND reactor neutrino experiment The Kamioka liquid scintillator antineutrino detector (KamLAND) is located in the same mine as the Super-Kamiokande detector. It measures the oscillation of $\bar{\nu}_e$ from 16 nuclear power plants with a power-weighted baseline of 180 km. Due to the relatively long baseline, the KamLAND detector can be sensitive to the solar oscillation parameters with $\Delta m^2 \sim 10^{-5}$ eV^2 which corresponds to the third term in (1.39). The result from KamLAND gave the first definitive evidence for $\bar{\nu}_e$ disappearance[36].

In summary, neutrino oscillations have been discovered in atmospheric and solar neutrinos and have been confirmed in both accelerator and reactor experiments. The three-flavor neutrino oscillations emerged from the experimental results. The atmospheric oscillation parameters have been measured by the high statistics data from the Super-Kamiokande detector to be $\sin^2\theta_{23} \sim 1.0$

and $\Delta m^2_{32} \sim 2.5 \times 10^{-3}$ eV^2. The solar oscillation parameters have been found by a combined fit of global solar neutrino experiments and KamLAND experiment to be $\theta_{12} \sim 37^0$ and $\Delta m^2_{21} \sim 7.6 \times 10^{-5}$ eV^2. The third mixing angle, θ_{13}, is constrainted by the CHOOZ reactor result to be small, $\sin^2 2\theta_{13} < 0.1$ at the best-fit Δm^2_{23} from atmospheric neutrino oscillations. It is interesting that two of the mixing angles are large, one nearly maximal, while the last one is small. The next logical step in exploring the mixing matrix using neutrino oscillations is to measure this last mixing angle. The work presented in this thesis contributes to the effort to measure one of the dominant backgrounds to the measurement of this angle by the T2K experiment. The T2K experiment and its physics goals are described in the next chapter.

Chapter 2

Overview of the T2K experiment

2.1 Introduction

In recent years, major progress has been made in neutrino physics, especially with regard to neutrino masses and neutrino oscillations. The neutrino oscillation results require that neutrinos are massive and there are at least three distinct masses. Two mixing angles (θ_{12}, θ_{23}) have been found to be large with θ_{23} almost maximal. However, the neutrino oscillation between the first and the third generation has not been found. Currently the mixing angle θ_{13} is constrained to be small ($\sin^2 2\theta_{13} < 0.17$) from the CHOOZ reactor experiment[23]. It is interesting to see if this mixing angle is nonzero.

T2K (Tokai-to-Kamioka) experiment is a second generation long baseline neutrino oscillation experiment to measure oscillation parameters, especially the mixing angle θ_{13} through ν_e appearance from a ν_μ beam[37]. The T2K neutrino beam is generated using the high intensity 50 GeV proton synchrotron at J-PARC in Tokai, Japan and the far detector is Super-Kamiokande which is located 295 km from the accelerator. The near detector which measures the neutrino beam properties before oscillation is installed 280 m from the target. The schematic of the J-PARC facility showing the accelerators and neutrino beam line is in Fig. 2.1 We will briefly describe the components of the experiment in the following sections. A detailed description of ND280 near detector can be found in the T2K ND280 conceptual design report[38].

2.2 T2K physics goals

The T2K experiment aims to measure the mixing angle θ_{13} through ν_e appearance. It has been seen that the appearance probability (1.33) also depends on the atmospheric oscillation parameters ($\Delta m^2_{23}, \sin^2 2\theta_{23}$). For this reason,

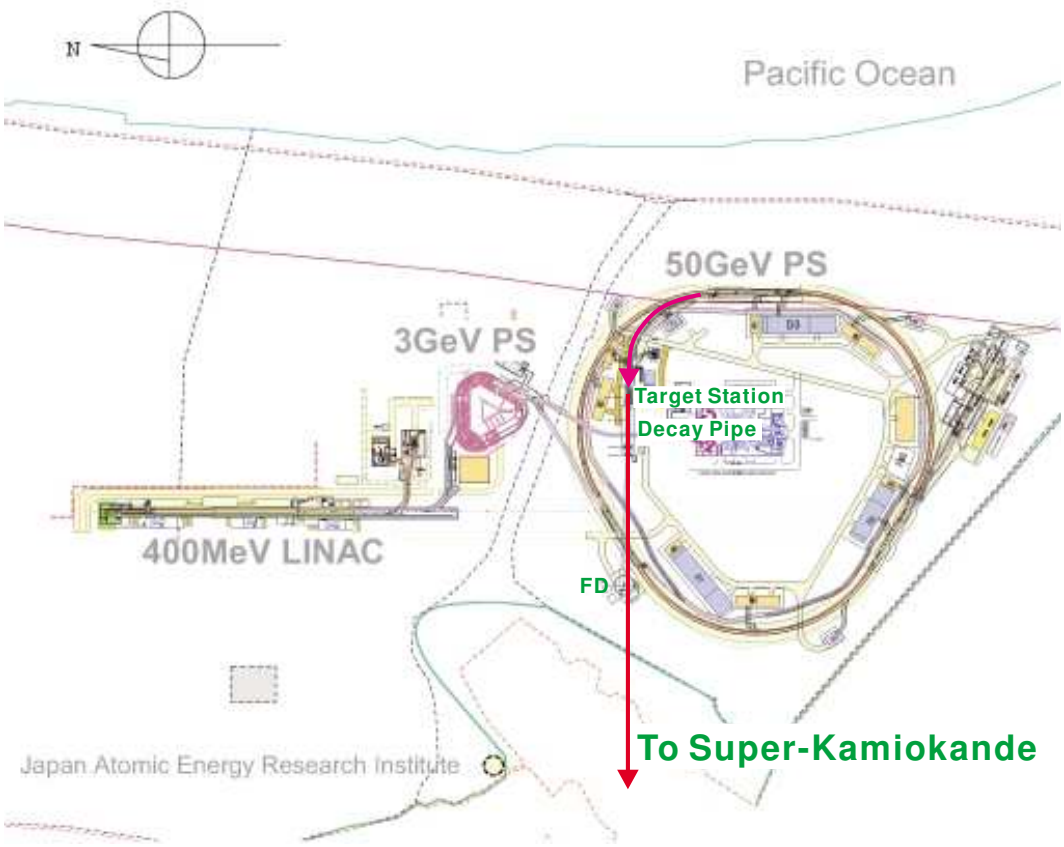

Figure 2.1: Layout of the J-PARC facility.

the T2K experiment will make precision measurement of these oscillation parameters and the mixing angle θ_{13}.

ν_μ disappearance

The oscillation parameters $(\Delta m^2_{23}, \sin^2 2\theta_{23})$ will be determined from the survival probability of ν_μ after traveling 295 km. This probability can be measured by comparing the neutrino spectra at the near and far site. The neutrino spectrum at the near site is measured by the near detector system. The neutrino flux is also measured at the near site and extrapolated to the far site to obtain the correct rate normalization. At the far site, the neutrino spectrum is measured by the Super-Kamiokande detector. Muon neutrinos are detected at Super-Kamiokande using the quasi-elastic charged current interaction which has better energy reconstruction. The muons are identified by the presence of a muon-like ring.

ν_e appearance

The mixing angle θ_{13} is determined from the measurement of the ν_e appearance signal. The ν_e signal comes from $\nu_\mu \rightarrow \nu_e$ oscillation if the mixing angle θ_{13} is nonzero. Electrons from ν_e quasi-elastic charged-current interactions are detected by the presence of a electron-like ring. Backgrounds from ν_μ interactions are further reduced by requiring that there is no decay electron. After this, there are two main backgrounds to the ν_e search at Super-Kamiokande: the background from single π^0 from neutral current interactions and ν_e intrinsic to the beam. The number of expected signal ν_e and backgrounds assuming 5×10^{21} protons on target (POT) at 50 GeV are shown in Table. 2.2. The dominant backgrounds are measured by the near detector system before oscillation and extrapolated to Super-Kamiokande. The estimated π^0 and intrinsic ν_e backgrounds are subtracted from the selected ν_e events. The final appearance signal is fitted to the appearance probability (1.1) to find $\sin^2 2\theta_{13}$. Fig. 2.2 shows the T2K sensitivity to θ_{13} at 90% confidence level as a function of Δm^2_{23}, assuming no CP violation ($\delta_{CP} = 0$) and normal mass hierarchy. The beam is assumed to be running at 750 kW for 5 years (or equivalently, 5×10^{21} POT at 50 GeV) and using 22.5 kton fiducial volume of Super-Kamiokande detector.

Table 2.1: Number of events and reduction efficiency of "standard" 1ring e-like cut and π^0 cut for 5 year exposure (5×10^{21} POT). In the calculation of oscillated ν_e, $\Delta m^2 = 0.003$ eV^2 and $\sin^2 2\theta_{13} = 0.1$ are assumed[37].

Off-axis angle 2^0	ν_μ CC	$\nu_\mu NC1\ \pi^0$	Beam ν_e	Signal ν_e
Generated in F.V.	10713.6	4080.3	292.1	301.6
1R e-like	14.3	247.1	68.4	203.7
e/π^0	3.5	23.0	21.9	152.2
$0.4 < E_{rec} < 1.2$ (GeV)	1.8	9.3	11.1	123.2

2.3 Neutrino beam and monitor

The neutrino beam is produced by smashing protons from the J-PARC proton synchrotron on a target. The main synchrotron is designed to accelerate protons up to 50 GeV, however, the initial proton energy is limited to 30

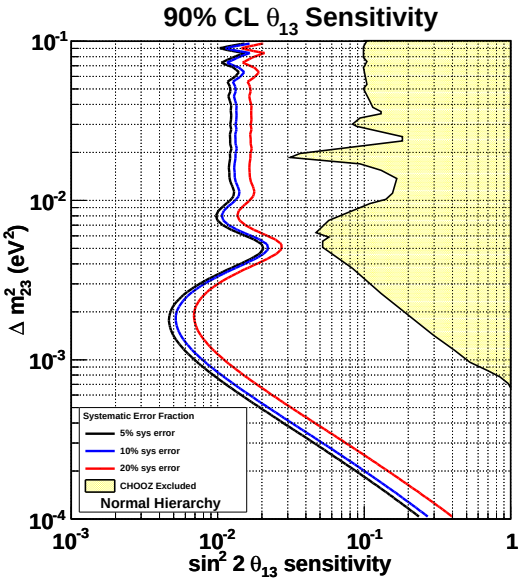

Figure 2.2: T2K sensitivity to θ_{13} at the 90% confidence level as a function of Δm^2_{23}. Beam is assumed to be running at 750kW for 5 years (or equivalently, $5{\times}10^{21}$ POT), using the 22.5 kton fiducial volume SK detector. 5%, 10% and 20% systematic error fractions are plotted. The yellow region has already been excluded to 90% confidence level by the CHOOZ reactor experiment. The following oscillation parameters are assumed: $\sin^2 2\theta_{12} = 0.8704$, $\sin^2 2\theta_{23} = 1.0$, $\Delta m^2_{12} = 7.6 \times 10^{-5}\mathrm{eV}^2$, $\delta_{CP} = 0$, normal hierarchy.

GeV. The proton beam is extracted by the neutrino primary beamline. The neutrino beamline consists of 28 combined function superconducting magnets which produce both dipole and quadrapole fields and normal magnets near the final focusing sections. The design intensity of the proton beam is 3.3×10^{14} at the rate of about 0.3 Hz. The target is a graphite cylinder of 30 mm in diameter and 900 mm in length. Three electromagnetic horns are used to focus (and select the right charge sign) charged pions generated in the target to the forward direction. The target is installed inside the inner conductor of the first horn to effectively collect and focus the pions. These horns are driven by a pulsed current of 320 kA synchronized with the beam. The focused pions decay into ν_μ and muons in a 110 m decay tunnel which follows the horns. There is a small fraction of ν_e (about .5% at peak energy) produced by decaying muons and kaons. The decay tunnel is filled with 1 atm helium gas to reduce pion absorption and tritium production. Charged particles are stopped by the beam dump placed at the end of the decay tunnel. The beam

dump is designed to allow high energy muons (> 5 GeV) passing through. These muons are used to monitor the conditions of the primary proton beam and the horn system.

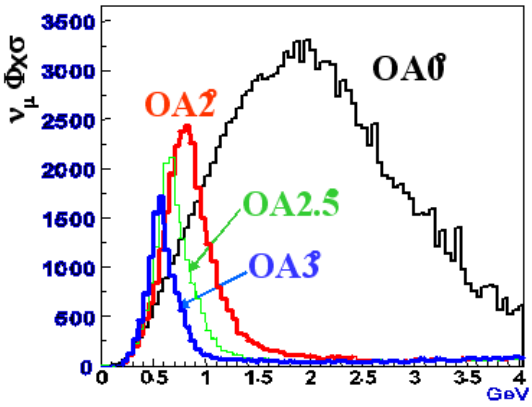

Figure 2.3: Neutrino energy spectra at SK at different off-axis angles, 3^0, 2.5^0, 2^0 and on-axis.

The T2K neutrino beamline adopts an off-axis beam configuration[39]. It exploits the kinematics of pion decay that the neutrino energy is not strongly dependent on the pion energy at a fixed decay angle in the lab frame to produce a narrow-band beam (Fig. 2.3). The narrow-band beam is desired to maximize the neutrino flux at energies near the first oscillation maximum. The off-axis angle can be changed from 2.0 to 2.5 degrees. This corresponds to the mean neutrino energies from 0.5 to 0.7 GeV. The nominal off-axis angle is 2.5 degrees, corresponding to the peak beam energy of about 0.7 GeV. The schematic of the T2K neutrino beam is shown in Fig. 2.4.

Because of the off-axis beam configuration, the neutrino spectrum at Super-Kamiokande is sensitive to the neutrino beam direction. For this reason there are two detector systems designed specifically for online neutrino beam monitoring: One is a muon monitor and the other is an on-axis neutrino detector. The muon monitor can measure the neutrino beam condition in real time by detecting the accompanying muons. The on-axis neutrino detector monitors the neutrino beam directly using neutrino interactions. The muon monitor and the on-axis neutrino detector are described below.

2.3.1 Muon monitor (MUMON)

The muon monitor is placed downstream of the beam dump and monitors the direction, profile, time structure, and intensity of the beam by detecting

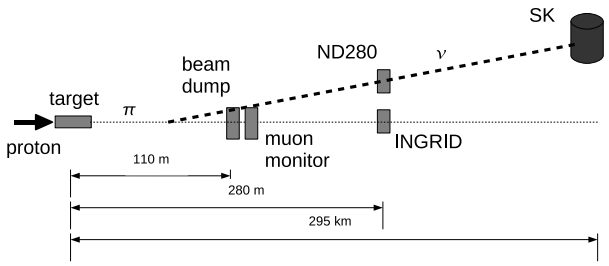

Figure 2.4: A schematic of the T2K neutrino beam. The T2K neutrino beam line uses an off-axis beam configuration where the neutrino beam is sent 2.5 degrees beneath the axis between the Super-Kamiokande detector and the decay pipe.

high energy muons which are produced together with the neutrinos. Thanks to the high muon flux, the MUMON is sensitive to the proton hit position on the target and the status of the target and horns. Therefore, it is also used as a proton beam monitor, a target monitor, and a horn monitor. The measurements of MUMON can monitor the quality of the neutrino beam on a spill-by-spill basis. Finally, the MUMON helps aim the neutrino beam at Super-Kamiokande during the beginning of the experiment. The MUMON consists of two independent detectors: a matrix of silicon detectors and an array segmented ionization chambers. Each detector covers an area of 1.5m $\times$ 1.5m. The silicon detector matrix consists of 7 $\times$ 7 silicon photodiodes mounted on the upstream panel. The silicon photodiodes are not radiation hard and can only be used in the early stage of the experiment. More radiation tolerant detectors like diamond detector are being tested. The ionization chamber detector consists of an array of 7 segmented ionization chambers on the downstream side.

2.3.2 On-axis detector (INGRID)

The INGRID detector is located on-axis at 280 m from the target and beneath the off-axis detector. It monitors the neutrino beam by using muons from charged current neutrino interactions. Because of the small neutrino cross sections, it can only monitor the neutrino beam on a daily basis. The total number of neutrino events observed by INGRID is about 10,000 events/day. The detector consists of 16 modules arranged in 7 vertical and 7 horizontal modules and two off-axis modules. Each module has dimensions of 1.2m $\times$ 1.2m $\times$ 1.3m and consists of 11 scintillator planes alternating with 10 iron targets. On the top and sides of each module, three or four additional scintillator

layers are used as a veto. Each tracking plane has 24 rectangular scintillator bars, each of dimensions of 5cm×120.3cm×1cm. A schematic view of the INGRID detector is shown in Fig. 2.5. Black boxes are the detector modules and red frames are supporting structure.

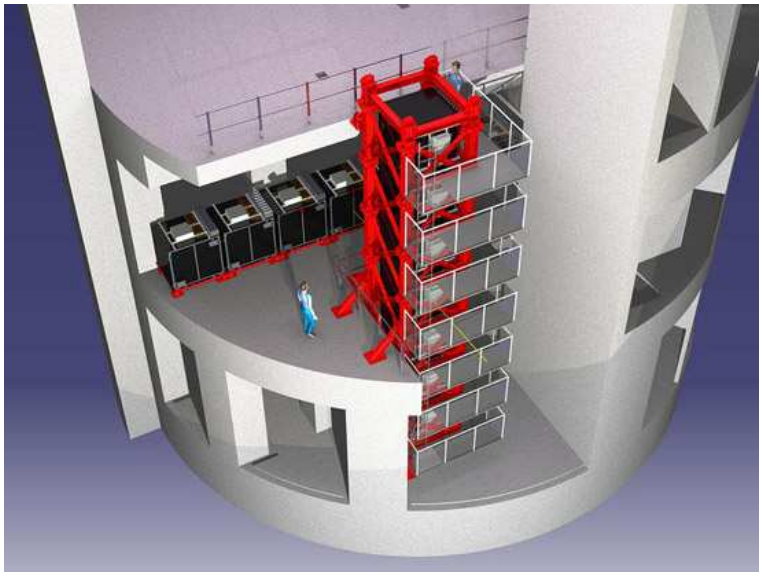

Figure 2.5: A schematic of the INGRID detector. Black boxes are the detector modules arranged in a cross.

2.4 Near detector system (ND280)

The near detector system is located off-axis at 280 m from the target and consists of different sub-detectors. The main purpose of the near detector system is to measure the properties of the neutrino beam before oscillation:

- Measure the neutrino flux and spectrum
- Measure different interaction cross sections to estimate the backgrounds at Super-Kamiokande.
- Measure the ν_e beam contamination for ν_e appearance search.

The ND280 sub-detectors are enclosed inside the UA1 dipole magnet operating at nominal 0.2 T (Fig. 2.6). The magnetic field is used to reduce electron diffusion inside the time projection chambers and bend charged particle trajectories for momentum measurement. The sub-detectors are described below.

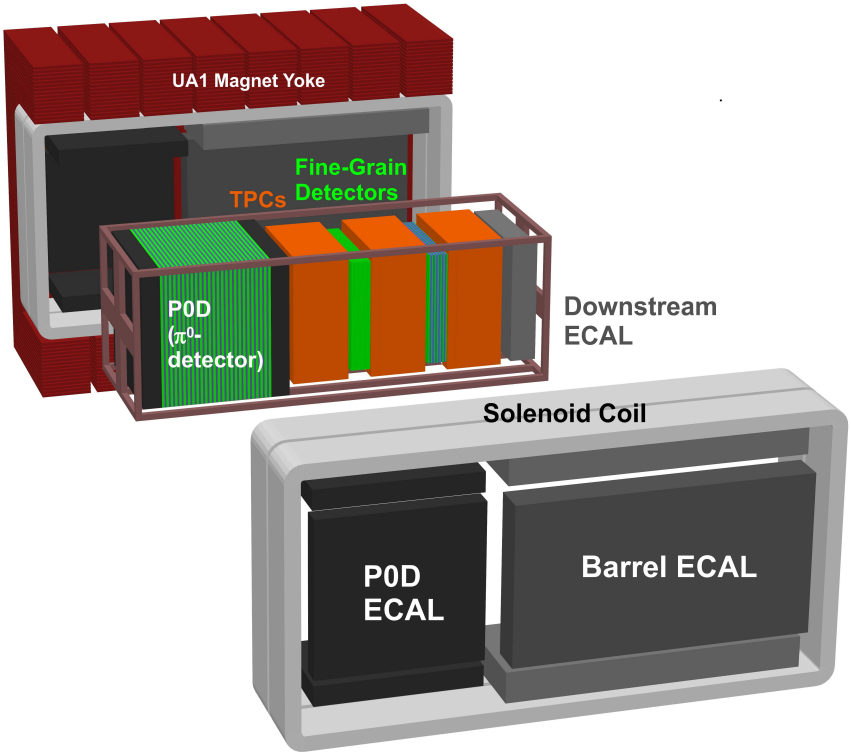

Figure 2.6: The off-axis near detector system shown with one side of the UA1 magnet. The inner detectors are supported by a basket and consist of the P0D upstream, followed by the tracker, and the downstream ECAL. They are surrounded by the side ECALs.

2.4.1 Pizero detector (P0D)

One of the dominant backgrounds to the ν_e appearance search in a water Cherenkov detector is single π^0 from neutral current interactions. The P0D is designed to measure the neutral current single π^0 production cross section on water. Using this cross sections, the π^0 background at SK can be estimated. The P0D consists of a water target sandwiched between two electromagnetic calorimeters (ECAL). The water target section consists of 26 tracking modules alternating with water modules. Each water module has two water bags supported by high-density polyethylene frame. Each tracking module is a complete tracking unit of dimensions of 220cm×230cm×3.9cm and it has x-y tracking planes perpendicular to the beam direction. Each tracking plane consists of triangular plastic scintillator bars, each of 1.7 cm height and 3.4 cm

base and has a axial hole at the center. The plan is to measure the single π^0 production in water-in and water-out modes. Events measured with water out are statistically subtracted from those with water in to obtain the production cross section on water.

2.4.2 Tracker: Fine-grained detector and time projection chamber

The other dominant background to the ν_e appearance search is the ν_e beam contamination which is about 0.5% of the ν_μ flux at peak energy. This background is resulted from kaon and muon decays, it can not be removed from the ν_μ beam and must be measured by the near detector. One of the purpose of the tracker is to measure this background. The tracker also measures ν_μ flux and spectrum before oscillation for ν_μ disappearance study.

Finally, in addition to the flux and spectrum measurement, the tracker can distinguish the simple quasi-elastic charged current interaction from non-elastic interactions. In the fine-grained detector, this is accomplished by the fine segmentation which allows tracking of low energy protons. The presence of both proton and muon tracks create a kinematical constraint to remove non-elastic events. Furthermore, the good particle identification of the time projection chambers using ionization energy loss can distinguish electrons, muons, and protons. The time projection chambers can also measure the charge sign of charged particles to further reject non-elastic events.

Fine-grained detector (FGD)

There are two FGDs, each of dimensions of 200cm × 200cm × 30cm. One FGD consists of 30 tracking planes. These tracking planes are arranged in alternating vertical and horizontal direction perpendicular to the beam. The back FGD consists of alternating x-y tracking planes and 3 cm thick layers of water target. For both FGDs, each scintillator plane consists of 200 scintillator bars, each of dimensions 1.0cm × 1.0cm × 200cm, has a central hole for wavelength shifting fiber and TiO_2 coating. The fine-grained segmentation allows tracking of low energy protons to distinguish CCQE and non-elastic events. Light collected by the wavelength-shifting fiber is read out by a MPPC.

Time projection chamber (TPC)

The TPCs are optimized to measure charged particles from neutrino interaction in the FGDs and the P0D. There are three TPCs sandwiching with the FGDs, with one TPC downstream of the P0D. Each TPC module has a

dimensions of 180cm × 200cm × 70cm (sensitive volume). It has a double wall structure, the inner wall makes up the field cage and the outer wall is used for gas, high voltage insulation. The sensitive volume contains a mixture of gases Ar-CF_4-iC_4H_{10} (95%-3%-2%) and has drifting velocity of 7.8cm/μs at 280 V/cm. Gas amplification and readout using Micromegas with pad size of 7mm × 10mm.

2.4.3 Electromagnetic calorimeter (ECAL)

Electromagnetic calorimeters surround the P0D and the tracker to detect showering (e^-, γ) particles from neutrino interactions in these detectors. Charged particles are produced and tracked by the inner detectors. However, because of the low mass of the inner detectors, showering particles can escape and cause energy leakage which reduces the energy resolution. The ECALs are designed to have a short effective radiation length to convert these particles. Showers found in the ECALs are matched to tracks or showers found in the inner detectors. The shower-to-track matching helps distinguish muons from electrons while the shower-to-shower matching reduces the energy leakage. Furthermore, the ECALs also improves the π^0 detection efficiency by increasing the probability of catching the γs from π^0 decay. Finally, the ECALs also acts as a veto detector to detect particles from neutrino interactions in the magnet.The ECALs consist of alternating layers of plastic scintillator and lead.

2.4.4 Side muon range detector (SMRD)

It is important to measure muon at high angle relative to the beam direction to increase the acceptance. As the name implies, the SMRD measures muon range from which the momentum can be estimated. The SMRD also acts as the veto detector for cosmic ray muons and is used to form the cosmic trigger. The SMRD is constructed by inserting scintillator detectors into the gaps between iron plates of the magnet.

2.5 Far detector - Super-Kamiokande

The far detector Super-Kamiokande (SK) is located 295 km from the near detector at the Kamioka Observatory, Gifu, Japan. Detailed description and analysis of the detector can be found in [40, 41]. A brief description is given here. SK is a 50 kton water Cherenkov detector. The detector is a cylindrical

tank of 41.4 m in height and 39.3 m in diameter. The tank is optically divided into an inner detector of 36.2 m in height and 33.8 m in diameter and an outer detector. Both sides of the dividing wall are mounted with photomultipliers (PMTs), 11146 20-inch diameter PMTs on the inside facing inward and 1885 8-inch diameter PMTs on the outside facing outward. Cherenkov light from particles are recorded by these PMTs. A schematic of the Super-Kamiokande detector is shown in Fig. 2.7.

The detector can distinguish electron from muon by looking at the light distribution of the projected Cherenkov cone. Electrons scatter more than muons, thus making a fuzzy ring. It is well-known that water Cherenkov detector can not distinguish between gamma and electron since they both produce e-like ring. Because of this, SK could mistake π^0 for electron when the two γs from the π^0 decay have a small open angle or large energy asymmetry. In the case of small open angle, the two γ's look like a single γ and in the case of large energy asymmetry, the smaller energy γ is not detected.

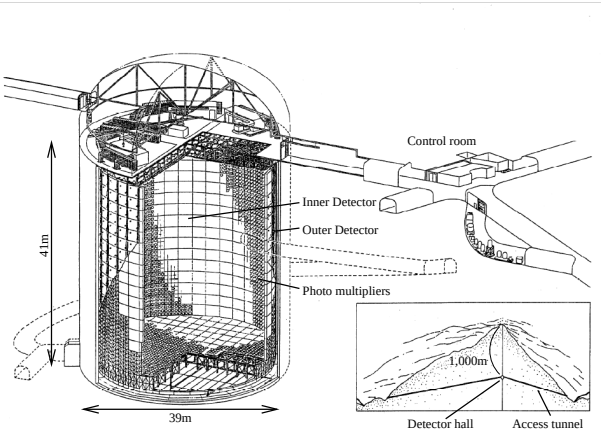

Figure 2.7: Schematic of the Super-Kamiokande detector.

Chapter 3

The P0D detector

One of the dominant backgrounds to the ν_e appearance search in a water Cherenkov detector is single π^0 from neutral current interactions. The P0D is designed to measure the neutral current single π^0 production cross section on water. This cross section will be used to estimate the π^0 background at Super-Kamiokande. The plan is to measure the single π^0 events with water in and water out and then events measured with water out will be statistically subtracted from the events with water in to obtain the event rate on water.

The P0D is a sampling tracking calorimeter. It consists of alternating active tracking planes and layers of passive target. Only the energy deposit in the active region can be measured while in the dead materials it is invisible to the detector. This invisible energy deposit can be inferred from the visible one and accounted for by an absolute energy calibration constant. The calibration constant can be obtained from either test beam or quantities involving the absolute energy scale such as invariant mass. For the P0D, there is plan to measure the calibration constant using the π^0 invariant mass from a well reconstructed sample of charged current π^0 events. Each tracking plane measures the two-dimensional projection of particle trajectory. The xz and yz projections of the particle trajectory are measured by alternate tracking planes. A complete three-dimensional trajectory can be reconstructed by combining the two-dimensional measurements from both projection planes. In this chapter we will describe in details the components of the detector.

3.1 Mechanical detector

The P0D consists of a water target section sandwiched between two electromagnetic calorimeters (Fig. 3.1). The water target section consists of 26 tracking modules alternating with water modules. A brass sheet of the same

transverse dimensions as the tracking module and 1.6 mm of thickness is inserted between the tracking module and water module to promote the photon conversion. Each water module has two water bags mounted side by side vertically and supported by high-density polyethylene frame. The ECAL section, each at the front and back of the detector, has 7 tracking modules alternating with 4 mm thick lead radiators. Each tracking module is a complete tracking unit which has x-y tracking planes perpendicular to the beam direction. Each tracking plane is made of triangular plastic scintillator bars (126 bars along the x direction and 134 bars along the y direction), each of 17.25 cm height and 33.5 cm base and has an axial hole at the center. Scintillation light generated by passing particles is collected by a Kuraray Y-11 wavelength-shifting fiber inserted in the hole. The signal is read out at one end of the fiber by a Multi-Pixel Photon Counter (MPPC) while the other end is polished and mirrored. On the opposite side of the MPPCs, there are two back-to-back LEDs used to inject UV light into the wavelength-shifting fibers for calibration purpose.

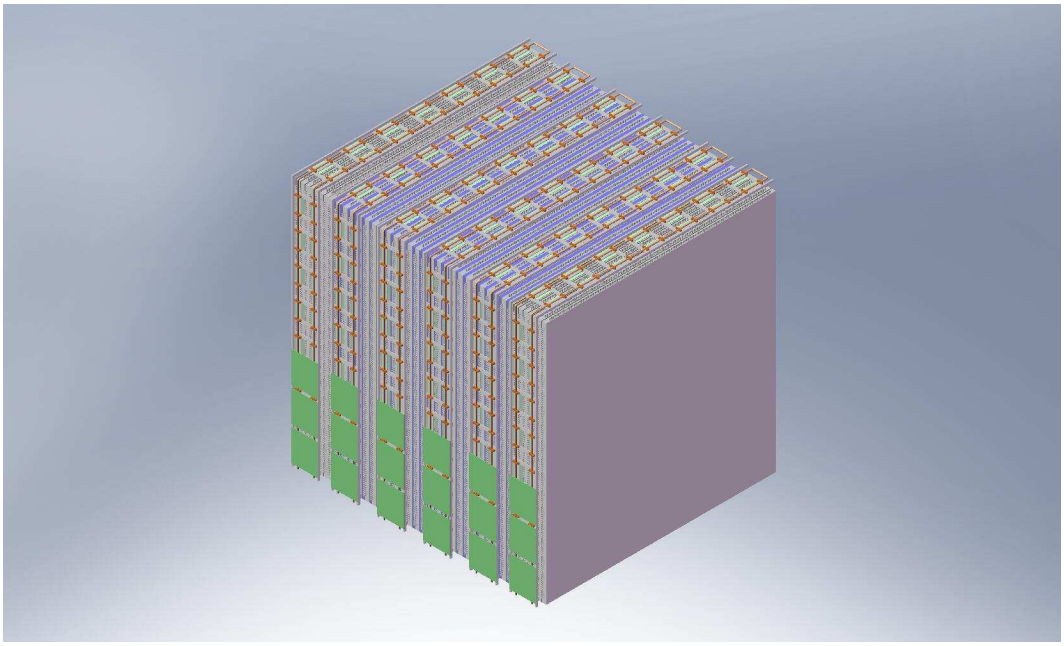

Figure 3.1: Engineer drawing of the P0D.

3.1.1 Tracking module (P0Dule)

Each P0Dule has of dimensions of 220cm(x)×234cm(y)×3.9cm(z). Each P0Dule consists of two tracking planes perpendicular to each other, one in the x

direction, the other in the y direction. The two scintillator planes are separated by a layer of epoxy which also keeps the two planes together. Both scintillator planes are fitted inside a PVC outer frame (3cm×3.85cm rectangular profile). Along the side of the PVC frame there are alignment holes which are used to mount the P0Dule into the final detector. There are also precision holes along the side for aligning the scintillator bars and protecting the photosensor housings. Both outer side of the scintillator planes are covered by a polystyrene skin of 1.5 mm thickness. The skins are glued to the scintillator planes by epoxy. At the positive +x and +y side, there are holes in the frame which allows the installation of MPPC housings. Figure 3.2 shows the P0Dule layout with the top skin removed, exposing two layers of scintillator bars arranged perpendicular to each other.

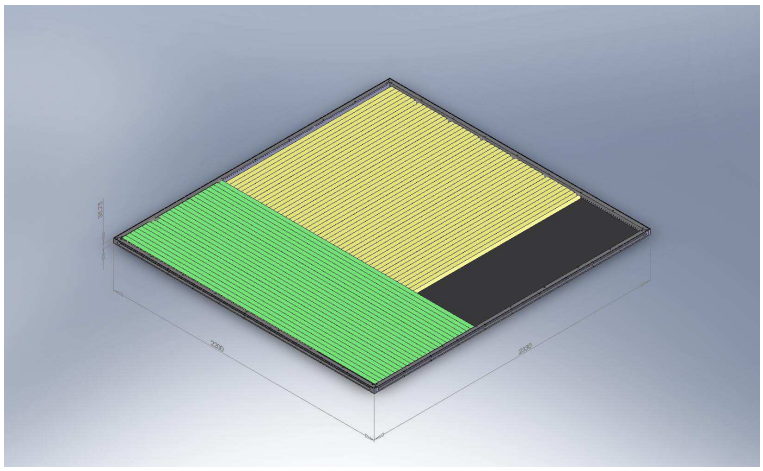

Figure 3.2: P0Dule layout, the top skin removed showing the two layers of scintillators.

3.1.2 Radiators

In the water target section, the radiator is a brass sheet of 1.6 mm thickness. For the ECAL sections, the radiator is made of rectangular lead sheets of 3.7 mm thickness fitted inside a stainless steel frame. The front and back of the radiator are supported by 0.5 mm thick sheets of stainless steel. The stainless steel sheets are glued to the lead by epoxy to provide support. The radiators in both ECALs and water target are supported in the final detector by the same threaded rods as the P0Dules.

3.1.3 Water target

There are 25 layers of water target. Each water layer has two water bladders made of high-density polyethylene (HDPE) fitted inside a HDPE frame. The bladders can be filled with water at the top. The depth of water in each bag is monitored with one pressure sensor and several binary level sensors.

3.2 Scintillator bars and wavelength-shifting fibers

Each tracking plane is formed from triangular plastic scintillator (polystyrene) bars, each bar of 1.7 cm height and 3.4 cm base. The bars in the x direction have the length of 2134 mm while the bars in the y direction have the length of 2274 mm. The bar has an axial hole of diameter 2.4-2.8 mm. The sides of the bar are coated with a layer of 0.25 mm of Ti_2O. Both ends of the bar are counterbored 5.2 mm in diameter and 20 mm deep for housing the optical ferrule at the photosensor side and the fiber guide at the light injection side.

A wavelength shifting fiber is inserted into the hole in the scintillator bar to collect scintillation light produced by passing particles. The Kuraray Y-11 multi-clad 1 mm in diameter WLS fibers are used. One end of the fiber is polished and mirrored by a 250 nm layer of 99.999% chemically pure aluminum for good reflectivity which is around 85%. The mirror is protected by a coat of epoxy. The other end of the fiber terminates in a precision alignment ferrule and is polished to an optical quality finish. The ferrule is glued to hole on the PVC frame to keep it from falling when in the vertical position. The photosensor is housed in an optical connector which is screwed to the frame. The optical connector in turn is snapped onto the ferrule to keep the photosensor in position. Figure 3.3 shows the WLS fiber terminating in the ferrule and connected to the photosensor, the whole structure is fitted in the hole on the PVC frame.

3.3 Photosensor

Photosensor converts the scintillation light collected by the WLS fiber into electric signal. The choice of photosensor is driven by the physics requirements such as gain and photon detection efficiency (PDE), overall detector design, and cost per unit because of the large number of channels in the detector ($\sim$ 54,000). First, since the off-axis near detector is enclosed inside the magnet,

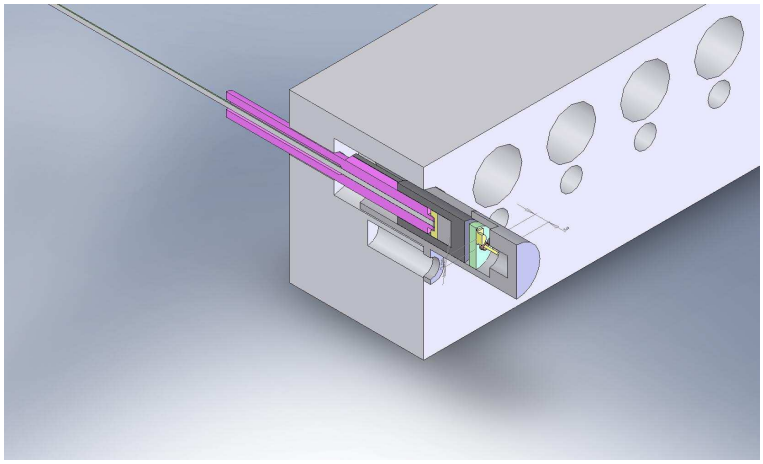

Figure 3.3: Bar readout

the photosensor chosen must be able to operate in a magnetic field. In addition, the limited space inside the UA1 magnet also constraints the choice of the photosensor. For these reasons, the T2K near detector uses the novel MPPC (Multi-Pixel Photon Counter) developed by Hamamatsu photonics[42]. Different operational characteristics of the MPPCs for the T2K near detector have been measured[43].

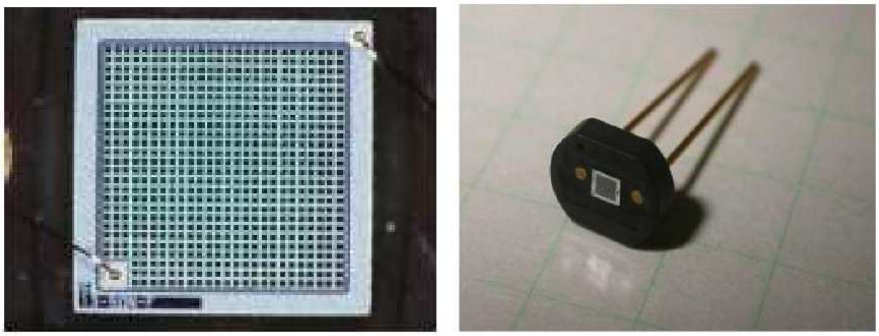

Figure 3.4: Photograph of a 667-pixel MPPC. Magnified surface of a MPPC (left) and a MPPC production package (right).

The MPPC is constructed from an array of avalanche photodiodes (APDs) operating in limited Geiger mode where the applied voltage is higher than the breakdown voltage. The magnified surface of an 667-pixel MPPC and a MPPC production package are shown in Fig. 3.4. Since the avalanche photodiode operates in Geiger mode, it has very high gain, 10^5-10^6. Each APD called

pixel acts as a binary detector. When a photon falls on a pixel of an MPPC, it creates an electron-hole pair. Due to the high gain, this electron-hole pair can trigger an avalanche and produces a sizeable output pulse which can be measured. The signals from all pixels are summed to a single output. The size of the output is proportional to the the number of pixels which fire and thereby the number of incident photons can be counted. A LED amplitude spectrum measured with MPPC is shown in Fig. 3.5. It can be seen that individual photoelectron peaks can be resolved. However, the high gain also causes a single thermal electron to produce measurable output. Therefore, the MPPCs can not distinguish real one p.e. event from dark noise.

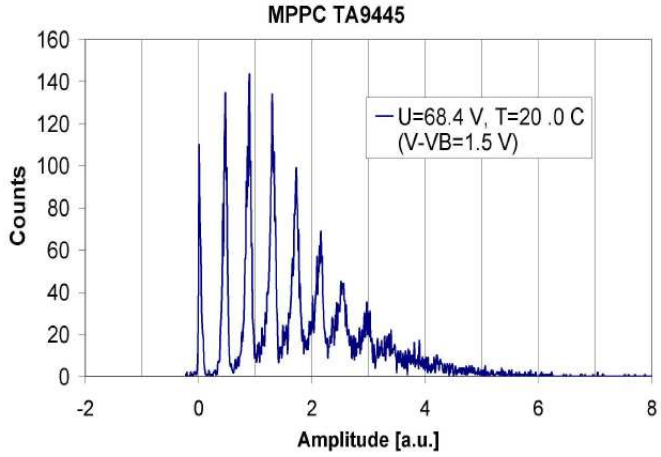

Figure 3.5: LED amplitude spectrum measured with the TA9445 MPPC at the bias voltage 68.4 V and the ambient temperature of 20^0C[43].

Typical operating voltage is about 1 V above the breakdown voltage or about 70 V. The difference between the operating voltage and the breakdown voltage is called overvoltage. Since the MPPCs are solid-state device, their gain is sensitive to temperature change. An increase in temperature raises the breakdown voltage which effectively reduces the overvoltage. A summary of the MPPC specifications and characteristics is given in Table 3.3.

There are noises inherent to the MPPCs: dark noise and correlated noise. The dark noise is caused by thermalelectron accelerated in the depletion region and has a typical rate of about 300-800 KHz. It is dominated by one photo-electron events, dark noise events above 1.5 p.e. is an order of magnitude

Table 3.1: Some specifications and characteristics of the MPPCs used in the T2K near detector.

Active area: 1.3 ×1.3 mm
Number of pixels: 667 (50×50 μm each)
Operation voltage: $\sim$ 70 V
PDE at 515 nm: $> 25\%$
Gain: 6×10^5 at $\Delta V \sim 1$ V
Dark noise rate: < 1.35 MHz
Operating in magnetic field (0.18-0.2 T)

less. The correlated noise is defined as secondary avalanche(s) produced by an original avalanche which could be triggered by either detection signal or one (equivalent) photoelectron from dark noise. While the dark noise is random and hence independent of the detection signal size, the correlated noise by definition depends on the signal. Therefore, understanding the effects of the correlated noise on the light output in different operating conditions will be crucial to the energy calibration. There will be more discussion of the MPPC noises and how to measure them in Chapter 6.

3.4 Electronics readout

The P0D detector uses the same front end readout system as other sub-detectors which uses the MPPCs as photosensors. The front end readout system for MPPC photosensors is based on the Trip-t chip originally developed at Fermilab for Visible Light Photon Counter (VLPC) readout in D0 experiment. There are 4 Trip-t chips on each front end board (TFB) which can instruments up to 64 MPPCs. The TFBs are read out and controlled by the Readout Merger Module (RMM) which provides communication with the data acquisition system (DAQ). Cosmic trigger primitives formed on TFBs from time coincidence of MPPC signals are sent to the Cosmic Trigger Module (CTM) where the programmable trigger decision can be made. Neutrino beam arrival time is transmitted to the TFBs through the Master Clock Module (MCM). Detailed description of the TFB and its performance with the MPPC photosensors are reported in [44]. Schematic of the readout system for MPPCs is shown in Fig. 3.6. Documentation of the RMM, CTM, and MCM are being written up by the electronics group and will be reported elsewhere.

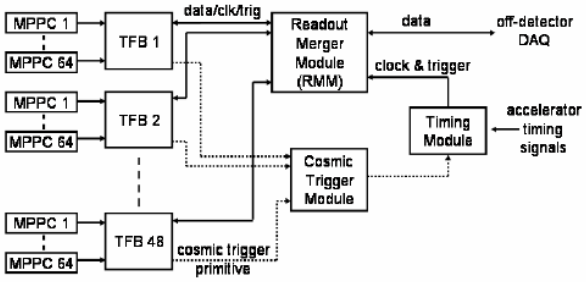

Figure 3.6: A schematic of the front end readout system for MPPC photosensors[44].

Chapter 4

Monte Carlo Simulation

At the near detector, the simulation is separated into different steps. It is a chain of these simulations: beam simulation, neutrino interaction simulation, detector simulation, and electronics simulation

- The beam simulation outputs the neutrino beam flux and the neutrino energy spectrum at the near detector site.
- The neutrino interaction simulation (event generator) simulates the neutrino interactions of the neutrino flux with the detector materials using the current knowledge of neutrino cross sections. It also transports particles produced at the neutrino interaction vertex through nuclear medium.
- The detector simulation transports the particles leaving the nuclei in the detector. It also provides a detailed description of the detector using realistic detector materials. Energy deposits in the sensitive volumes of the detector are saved.
- The electronics simulation converts the energy deposits from detector simulation into digitized hits in the same format as the actual data.

The beam simulation is maintained by the beam group and not described here.

4.1 Neutrino interaction simulation

The event generator simulates the interaction of the neutrino beam with the nuclei of the detector materials using the current knowledge of neutrino cross sections. It uses the simulated neutrino flux from the beam group and simulate the interactions of neutrino with detector materials. The event generator also simulates the transport of primary particles produced at neutrino interaction

vertex in the nuclear medium. The output of the generator for each neutrino interaction is a list of particles leaving the nucleus with their kinematics. In the T2K experiment, NEUT is chosen as the official generator[45].

The following neutrino interaction modes are included in NEUT

$$\nu + n \rightarrow l^- + p \tag{4.1}$$
$$\nu + n \rightarrow l^- + n + \pi^+ \tag{4.2}$$
$$\nu + n \rightarrow l^- + p + \pi^0(\eta) \tag{4.3}$$
$$\nu + p \rightarrow l^- + p + \pi^+ \tag{4.4}$$
$$\nu +^{16} O \rightarrow l^- +^{16} O + \pi^+ \tag{4.5}$$
$$\nu + N \rightarrow l^- + N + \text{multi}\pi \tag{4.6}$$
$$\nu + N \rightarrow l^- + N + \text{mesons} \tag{4.7}$$
$$\nu + N \rightarrow \nu + N \tag{4.8}$$
$$\nu + N \rightarrow \nu + N + \pi^0(\eta) \tag{4.9}$$
$$\nu + n \rightarrow \nu + p + \pi^- \tag{4.10}$$
$$\nu + p \rightarrow \nu + n + \pi^+ \tag{4.11}$$
$$\nu +^{16} O \rightarrow \nu +^{16} O \tag{4.12}$$
$$\nu + N \rightarrow \nu + N + \text{multi}\pi \tag{4.13}$$
$$\nu + N \rightarrow \nu + N + \text{mesons} \tag{4.14}$$

Nuclear effects are included for both initial state and final state particles. For initial nucleons, the nuclear potential, Fermi motion and Pauli blocking effects are taken into account. For $\nu^{16}O$ simulation, the momentum distribution of nucleons is estimated from electron ^{12}C scattering experimental data.

For nucleons and mesons in the final state, a cascade model is used to simulate their interactions before exiting the nucleus. The following processes are considered for mesons, especially pions: inelastic scattering, charge exchange, and absorption. A process is selected among the competing processes using their corresponding mean free paths. The calculated mean free paths depends not only on the pion momentum but also the pion position. For nucleons, the elastic scattering is simulated using cross sections from nucleon-nucleon scattering experimental data. Single-delta and double-delta production are also simulated using the isobar model. Finally, gamma production from de-excitation of nucleus is also included in the simulation.

The NEUT neutrino simulation was written for water Cherenkov detectors (Kamiokande, Super-Kamiokande), so it deals mostly with neutrino interactions on oxygen. As the time of writing, NEUT does not handle real the detector geometry, i.e., not following neutrino ray and simulating neutrino in-

teractions with nuclei along the path. For use in the reconstruction algorithm development, NEUT simulates neutrino interactions on oxygen, then neutrino vertices with final state particles are distributed throughout the detector using mass density.

Another event generator, GENIE, is also used at the near detector for cross check[46].

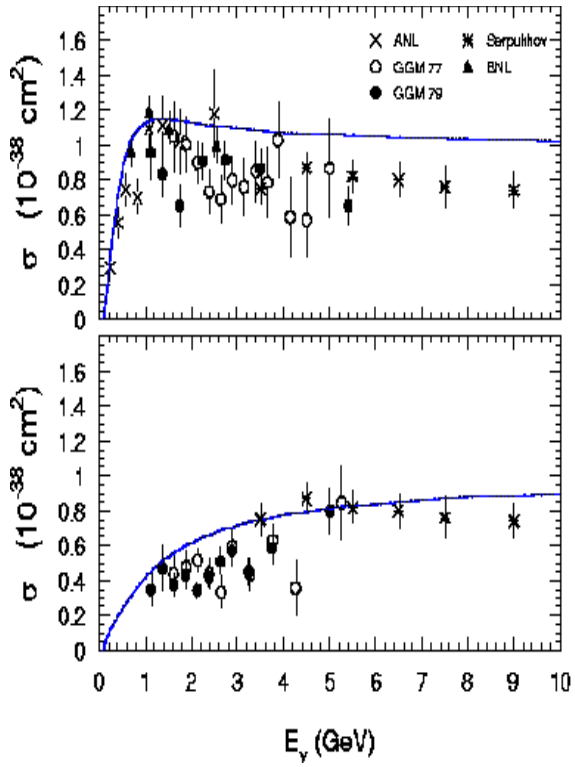

Figure 4.1: Cross sections of charged-current quasi-elastic scattering from NEUT simulation. Experimental data from different experiments are also shown for comparison[45].

4.2 Detector and electronics simulation

The detector simulation is based on Geant4 simulation package[47]. Geant4 is a software toolkit for the simulation of the passage of particles through matter. The detector simulation takes the particles with their kinematics from the event generator and transports them separately in the detector. It also provides a detailed description of the detector with realistic detector materials.

The energy losses of particles are simulated and energy deposits along the path lengths are saved in *hits*. Each hit keeps the position, timing, and the amount of energy deposit. Details of the simulation are described in the Geant4 documention.

The electronics simulation inputs hits from the detector simulation. The output of electronics simulation are hits in the same format as the actual experimental data and can be used by the reconstruction software (Chapter 6). It simplifies the scintillation process by generating a number of photons corresponding to the amount of energy deposit using a conversion factor. For example, a conversion factor of 50 photons/MeV means that an amount of 1 MeV energy deposit will generate 50 photons in the optical fiber. The number of photo-electrons is scaled by a factor which represents the light attenuation during propagation inside optical fiber to the photosensor. The light attenuation curve is assumed to have the form:

$$a(l) = (1 - f)e^{-l/c_s} + fe^{-l/c_l} \tag{4.15}$$

where c_s, c_l are the long, short attenuation components and l is the distance from the photosensor. The scaling factor is

$$a(l) + a(L - l)ra(L), \tag{4.16}$$

where r is the mirror reflectivity and L the fiber length.

Chapter 5

Event Reconstruction in the P0D

The detector provides the measurements of particle two-dimensional position, time, and energy deposit in terms of hits. Each hit contains position, timing, and energy deposit in the corresponding scintillator volume. The reconstruction of complete trajectories and kinematics of particles must be done by specialized algorithms using these hits. The interaction vertex can be estimated by extrapolating the reconstructed particle trajectories. This is called event reconstruction. The event reconstruction uses the fact that particles make characteristic hit patterns. Specifically, there are two distinctive hit patterns: charged particle track which appears as relatively straight line and electromagnetic showers created by γ or electron. This chapter presents the event reconstruction in the P0D.

5.1 Full-spill reconstruction

The detector readout electronics system is synchronized with the arrival time of the neutrino beam so that it can record neutrino data every time a spill comes. The neutrino data from one spill is stored in an *event*. Between the neutrino beam time, the readout electronics system switches to either cosmic or light injection calibration mode. Dependent on the beam configuration, a spill could have 6, 8, or 15 bunches. The Trip-t timing structure is set so that each bunch fits inside one Trip-t integration period. The hits produced by neutrino interactions in each event are separated into groups using the Trip-t timeslices, each corresponding to one bunch. Since there are more timeslices than bunches, the remaining timeslices after the spill time are used to store signals from muon decays. Each hit group is reconstructed independently except for the muon tagging step where the hits of the whole spill are used. In order to reduce noise hits from either the MPPC dark noise or slow neutrons

produced by neutrino interactions from the magnet, only hits within the first 100 ns window of each bunch are included in the reconstruction.

5.2 Charged particle track reconstruction

5.2.1 Track pattern recognition

The main task of the track pattern recognition is to detect charged particle tracks and separate them from showers. The charged particle tracks are mostly muons from charged current neutrino interactions. In the following we will describe the algorithm to detect and separate charged particle tracks from showers in 2D projection plane. The algorithm is applied separately on the xz and yz hits. Charged particle tracks which appear as relatively straight lines are detected using the Hough transform[48]. The Hough transform in its original form is a line detection algorithm. The normal equation of a straight line in two dimensions is

$$r = x\cos\theta + y\sin\theta, \tag{5.1}$$

where θ is the angle between the vector which is perpendicular to the line and the x-axis, and r is the distance from the line to the origin. In this representation each line in the image is defined by a point (r, θ). The (r, θ) plane is usually referred to as *Hough space*. Using (5.1), a point (x_0, y_0) in the image space can be mapped to a sinusoidal curve in the Hough space, $r(\theta) = x_0\cos\theta + y_0\sin\theta$. Two curves corresponding to two points in the image space intersect at (r, θ) in the Hough space. The intersection point (r, θ) defines the line that passes through both points in the image space. More generally, a set of points on a straight line in the image space corresponds to a set of curves that intersect at the point (r, θ) in the Hough space. Therefore, the detection of a straight line in the image space becomes detecting the coordinates (r, θ) where most sinusoidal curves pass through. To detect this point (r, θ), the Hough space is discretized into cells. Then for each point (x_0, y_0) in the image space, a vote is added to cells (r_i, θ_i) in the discretized Hough space, where r_i is a discrete value given by (5.1) and θ_i running from 0 to 2π. This is done for all points in the image space. Finally, the cell with the most votes gives the detected line in the image space.

Although the Hough transform is a robust line detection algorithm, it has certain drawbacks. First, it is a global transformation which means that points are found to belong to a straight line can be far away from each other. This is undesired for tracking application since the hits from the same particle

trajectory also belong to a spatial cluster. Second, it is hard to find optimal discretizing step for r and θ. If these steps are too small, points that deviate slightly from the line will not be detected, the contributing votes falling into neighboring cells. The cells in the neighborhood of the cell with the maximum votes can give spurious lines. On the other hand, if the steps are too wide, different lines can be detected as a single line.

The six points on a straight line in the image space and their corresponding curves in the Hough space is shown in Fig. 5.1. Since the points are strictly on a line, the curves intercept at a single point. In practice, the intercepting point has finite size.

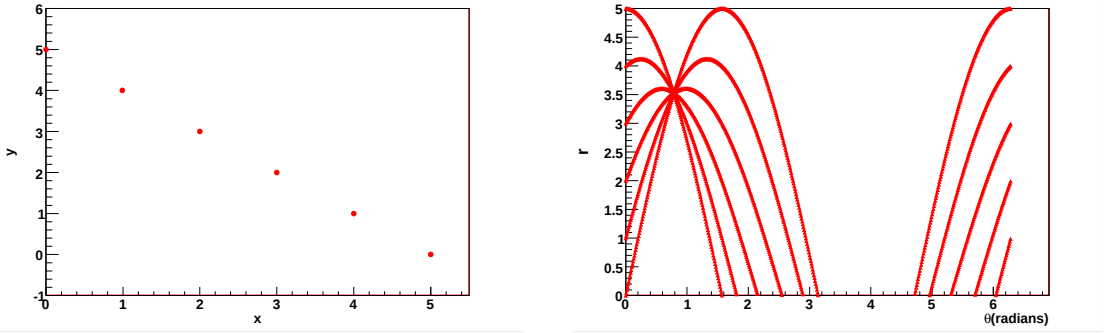

Figure 5.1: Illustration of the Hough transform. Each point in the image space on the left is mapped into a sinusoidal curve in the Hough space on the right. The curves from the points on a straight line in the image space intercept at a single point in the Hough space.

Application of the Hough transform

Charged particle tracks are found independently in the xz and yz projections. Let us consider the track finding algorithm in one projection using either xz or yz hits. The Hough space is discretized into $(2^0, 3$ cm) cells. The r step is chosen to detect charged particles at normal incidence to the scintillator plane. Particles with some angle with respect to the z-axis have smaller track width than the normal incident particles ($w \rightarrow w \cos\theta$, where θ is the angle between the track and the beam z axis). Since there could be more than one charged particle tracks in an event, the following steps are applied repeatedly to search for all the tracks.

- The largest rectangle which contains all the hits are found using hit positions, this defines the size of the image space. This is to improve computational performance, one could use the detector size.

- For each hit with the two dimensional position (x_0, y_0), votes are added to cells (r_i, θ_i) given by (5.1). In practice, the two dimensional hit position is either (x, z) or (y, z) in the detector coordinate system.

- Find the cell with the maximum number of votes. The hits in the image space that contribute votes to this cell are assigned to a straight line defined by the cell coordinates (r_{max}, θ_{max}). These hits form the raw charged particle track.

- Since the Hough transform is global, these hits may be far away from each other. Therefore, a density-based clustering [49] is applied. This ensures that hits associated to the track are spatially connected. The output of the density-based clustering is a set of clusters, each having a list of hits associated with it. Only the cluster with the most hits is kept and hits belonging to other clusters or hits not associated with any cluster are returned to the remaining hit list.

- If a track is slightly bent, the Hough transform could find only short straight segments of the track. This can be avoided by increasing the r discretizing step. However, a wider r step means that showers with small width can be mis-identified as tracks. Therefore, the r step is kept at 3 cm and the track is extended at both ends using a track following algorithm (see below).

- All hits belonging to the detected track are removed.

The steps are repeated until there are no remaining hits or the number of remaining hits is below a threshold of five hits. After this step, there is a set of charged particle track candidates and a set of remaining hits which are not associated with any track.

Track following

A track following algorithm is used in combination with the Hough transform to find charged particle tracks. The algorithm is applied at both ends of the track candidate found by the Hough transform. The track following algorithm at one end is described as follows. First, the five scintillator planes at the end of the track is selected. Next the position of the hits from these planes are fitted to a straight line. The fitted line is projected to the next plane away from the track end. If there are no hits within a window of 4 cm around the projected point on this plane, the track following is stopped. If there are hits within the window, then the plane are added to the five existing

planes. The last plane at the other end is removed. The steps are repeated with the new five planes. When the track following at one track end stops, it is applied at the other end.

Charged particle track and shower separation

The tracks are called candidates because they could be part of a large shower. The candidates have to pass one of the following selection criteria to become tracks:

- If the track has a segment longer than 40 cm with no hits in the neighborhood.
- If the *track width* is less than 1.2 cm. The track width is calculated as follows. For track traversing more than five scintillator planes, it is broken into five scintillator plane segments. A principal component analysis (PCA) is performed on each segment. The PCA finds the principal axis along which the covariance is maximized. The second principal axis which is perpendicular to the principal axis is along the width of the segment. The coordinates of hits on this axis characterize the width of the segment. The standard deviation of this coordinate of all track hits in this segment is defined as the track width.

The hits which are not associated with any charged particle track are passed to the π^0 reconstruction.

5.2.2 Track matching

The P0D measures particle trajectory in the xz and yz plane independently. Three-dimensional track must be reconstructed in software using these two-dimensional measurements. The matching is proceeded in the following steps:

- All tracks in the xz plane are paired up with all tracks in the yz plane. Let m, n be the number of charge particle tracks in the xz, yz plane, respectively, then there are $m \times n$ pairs.
- For each pair, the z offsets between two tracks at both ends , $\Delta z_f, \Delta z_b$ are calculated. Only the pair with both Δz less than 10 cm are considered matched. The definition of Δz is illustrated in Fig. 5.2.
- All pairs are sorted using the total z offset, $\Delta z \equiv \Delta z_f + \Delta z_b$. The pair with the smallest Δz is considered matched.

- If two pairs have the same Δz, then the charge difference is calculated for each pair, and the pair with the smaller charge difference is considered matched.
- The two two-dimensional tracks corresponding to the matched pair are removed and the procedure is repeated.

The matched pairs are used to form three-dimensional tracks.

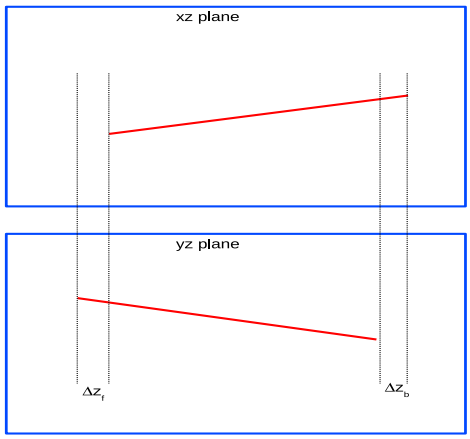

Figure 5.2: Illustration of track matching. The two-dimensional tracks are in red. The four vertical dashed lines indicate track ends

5.2.3 Track and vertex fitting

After track matching, each 3D track consists of both xz and yz hits. Track fitting uses these hits to calculate the best estimate of the particle trajectory and direction at each scintillator plane. Since the sensitive detector is made of triangular scintillator bars, a charged particle passing a scintillator plane makes two or three hits, depending on the incident angle. The estimated position on this plane is the energy-weighted position of these hits

$$\bar{x} = \sum_{\text{hits}} q_i x_i \tag{5.2}$$

where x_i is the position, $q_i = Q_i/Q_{tot}$ is the fractional energy. This energy-weighting procedure is done for each track plane before the track fitting.

The fitting is done using the discrete Kalman filter[50]. The dynamic model for the Kalman filter is straight trajectory with small random perturbation to the particle direction to account for multiple scattering. The discrete Kalman filter is a set of equations which provides a recursive solution to the state estimation problem. The filter not only gives an optimal state estimation but also can predicts the state using the dynamic model. The prediction can be used to extrapolate tracks in a detectors that measure the 2D projections of particle trajectories.

Application of the Kalman filter to track fitting

The state vector is defined as

$$\hat{x} = \begin{pmatrix} x \\ y \\ d_x \\ d_y \end{pmatrix} \tag{5.3}$$

where x, y are the particle position and d_x, d_y the x, y components of the direction vector, respectively. Note that the coordinates (x, y) here are either (x, z) or (y, z) in the detector coordinate system. The process equation which predicts the state vector at plane $k+1$ given the state vector at plane k is

$$x_{k+1} = F_{k+1,k} x_k + w_k \tag{5.4}$$

where $F_{k+1,k}$ is the transition matrix. For a straight trajectory, the transition matrix is given by

$$F_{k+1,k} = \begin{pmatrix} 1 & 0 & \Delta z & 0 \\ 0 & 1 & 0 & \Delta z \\ 0 & 0 & 1 & 0 \\ 0 & 0 & 0 & 1 \end{pmatrix} \tag{5.5}$$

where Δz is the z distance between planes k and $k+1$.

The measurement equation which relates measurements to the state vector is

$$z_k = H_k x_k + v_k, \tag{5.6}$$

where z_k is the position measurement at plane k and H_k is the measurement matrix. The position measurement can be either x for X scintillator plane or y position for Y scintillator plane. The measurement matrix is given by

$$H_k = \begin{pmatrix} 1 & 0 & 0 & 0 \\ 0 & 1 & 0 & 0 \end{pmatrix}, \tag{5.7}$$

where the last two columns are all zero since there is no direction measurement. The process noise w_k and the measurement noise v_k are assumed to be independent, zero-mean, and with normal probability distributions

$$\begin{aligned} p(w) &\sim N(0, Q) \\ p(v) &\sim N(0, R), \end{aligned} \tag{5.8}$$

where Q is the process covariance matrix and R measurement covariance matrix.

Initialize the filter

The first step is to estimate a state vector which serves as the initial state for the filter. The initial state vector is estimated as follows. Hits associated with the track are fitted to a straight line separately in xz and yz planes. The best fit line equations are

$$x = k_x z + b_x \tag{5.9}$$

$$y = k_y z + b_y, \tag{5.10}$$

where k and b are parameters determined from the fits. Note that each of these two equations is also a three-dimensional plane equation. The intersection of these two planes is a straight line which defines the particle trajectory. It gives an estimate of the particle trajectory in case the trajectory slightly deviates from the straight line. Let z_0 be z position of the starting point, then the three-dimensional point line equation at this point is determined by

$$\begin{aligned} &M_0(k_x z_0 + b_x, k_y z_0 + b_y, z_0) \\ &\qquad \vec{s}(k_x, k_y, 1). \end{aligned} \tag{5.11}$$

This point line equation is used as the initial state vector. Remember that a line equation in three dimensions can be written in the parametric form

$$\begin{aligned} x &= x_0 + l * t \\ y &= y_0 + m * t \\ z &= z_0 + n * t. \end{aligned} \tag{5.12}$$

In other words, any point on the line are defined by (5.12) given (x_0, y_0, z_0) and (l, m, n). The parametric form of a line in three dimensions is called point line equation.

Track parameter estimation

We will use the update step of the Kalman filter to estimate track point position and direction at every scintillator plane traversed by the particle. There are two state estimates in the Kalman filter: *a priori* state estimate and *a posteriori* state estimate:

$$\begin{aligned} \hat{x}_k^- &= F_{k,k-1}\hat{x}_{k-1} + w_{k-1} \\ \hat{x}_k^+ &= \hat{x}_k^- + K_k(z_k - H_k\hat{x}_k^-), \end{aligned} \tag{5.13}$$

where K_k is the Kalman gain matrix defined in the following. The first equation is called the prediction step or time update step and the second equation is called the measurement update step since it uses the measurement, z_k. Let $\hat{x}_0$ ($k = 1$) be the initial state vector, the prediction step gives the estimate of the state vector at the next scintillator plane. The update step uses the position measurement at the current plane to adjust the predicted state vector. This is supposed to be a better estimate since it takes into account of the position measurement. Note that the "-" superscript denotes the state (or covariance matrix) before using the measurement and the "+" after using the measurement. For k running from 0 to N, with N the number of scintillator planes that the particle passes through, the iterative formulae (5.13) gives the optimal estimate of all the track points. It is noted that since the measurements are only two-dimensional, the Kalman filter also includes extrapolating during the prediction step.

The Kalman gain matrix is given by

$$K_k = \frac{P_k^- H_k^T}{H_k P_k^- H_k^T + R_k}, \tag{5.14}$$

where $P_k^- \equiv F P_{k-1} F^T + Q_{k-1}$ is the *a priori* process covariance matrix, H^T the transpose of the measurement matrix, and R_k the covariance matrix of the measurement noise (5.8).

Forward-backward smoothing

Suppose that a particle passes through N scintillator planes, we have N independent measurements of the particle trajectory. Now we want to estimate the trajectory intersection point and the particle direction at scintillator plane m. The standard Kalman filter gives the optimal estimate of the state vector at plane m using the available position measurements from plane 0 to plane m. However, for track fitting the measurements from plane $(m + 1)$ to plane N are also available. Therefore, it is tempting to include these measurements to improve the state estimate at plane m. The forward-backward smoothing

is a way to obtain a better state estimate using all available measurements. It involves calculating two state estimates at the plane m. The first estimate, $\hat{x}_f$, is based on the standard Kalman filter with k running forward from 0 to m. The second estimate, $\hat{x}_b$, based on the standard Kalman filter with k running backward from N-1 to m. The forward-backward smoothing combines the two estimates to form the optimal smoothed estimate of the state vector

$$\hat{x} = K_f \hat{x}_f + (1 - K_f)\hat{x}_b, \tag{5.15}$$

where K_f can be calculated from the covariance matrices of the forward and backward estimates

$$K_f = \frac{P_b}{P_f + P_b}, \tag{5.16}$$

where we have dropped the "+" sign on the covariance matrices.

The track fitting procedure described above has been tested on a Monte Carlo sample of 10,000 2-GeV muons. The direction of the muons are limited to 10^0 from the z axis. During detector simulation, the true muon position and direction are saved every 1 mm. This is to compare the true position and fitted position at each scintillator plane. The muon MC sample is run through track pattern recognition, track matching and fitting. After track fitting, the muon position and direction at each scintillator plane are available. At each plane, we find the true trajectory point which is closest in z to the fitted track point. The fitted track point is then projected to the xy plane of the true trajectory point. The x, y positions of the true trajectory point are compared with those of the projected point. The x, y residuals are shown in Fig. 5.3. These residuals are fitted to a Gaussian function and it is found that the means are zero and standard deviations are $\sigma_x = 2.1$ mm and $\sigma_y = 2.0$ mm.

Vertex fitting

The vertex reconstruction is simple in neutrino experiments, especially for low energy neutrino beam like T2K since there are not many particles coming out of the vertex. Most of the time there is a single muon track from charged current interactions. In this case the interaction vertex is simply the most upstream track point. When there are more than two tracks, the vertex is found by minimizing the vertex distance to all the tracks

$$\sum_{\text{tracks}} \left| (\vec{r} - \vec{r_0}) - ((\vec{r} - \vec{r_0}).\vec{n})\vec{n}) \right|, \tag{5.17}$$

where $\vec{r_0}$ is the vertex position to be obtained from the minimization, $(\vec{r}, \vec{n})$ the point line equation of the track, and the sum is over all tracks. For the

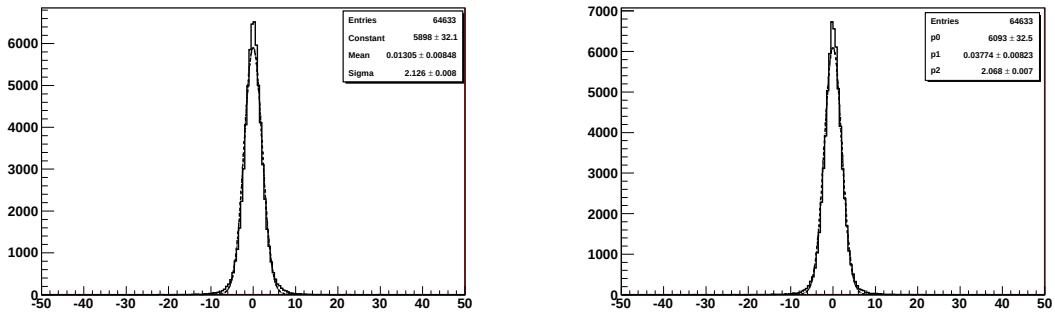

Figure 5.3: Residuals of track fitting (solid histogram) and Gaussian fitted curve (dashed line). The fitted parameters are $\mu_x = 0.0$ mm, $\sigma_x = 2.1$ mm and $\mu_y = 0.0$ mm, $\sigma_y = 2.0$ mm.

interaction channels where only the π^0 produces hits, e.g., $\nu_\mu + n \rightarrow \nu_\mu + n + \pi^0$, its vertex reconstruction is described in 5.6.

5.3 Particle identification

Since the main purpose of the P0D is to measure the π^0 spectrum and its production cross sections, it is crucial to reject as many charged-current neutrino interactions as possible. To do so requires to distinguish muons from protons. These two particles appear as charged particle track in the P0D. It is noted that since the charged pion mass is close to the muon mass, it is not possible to distinguish charged pions from muons in the detector. For example, these two interaction channels might have similar signature in the detector: neutral-current single π^0 production accompanied by a proton and charged-current single π^0 production where the proton is not detected. Another example which does not affect the neutral-current π^0 measurement, but important for cross section measurements, is the quasi-elastic scattering with both proton and muon tracks detected and the charged-current single charged pion production with the proton not detected. In this section we will describe the particle identification algorithm which distinguishes muons from protons using their energy deposit.

The P0D is a sampling detector, it does not measure all the energy losses by a charged particle, but only a fraction of the energy deposit on active scintillator planes. When a relativistic charged particle traverses the detector, it continuously loses energy through excitation or ionization of atomic electrons. Energy loss is a stochastic process, i.e., particles with the same initial

conditions lose different amount of energy when passing through the same scintillator layer. Therefore, energy deposits on a scintillator layer by a number of particles are not a discrete value, but a Gaussian-like distribution. This distribution is more skewed (Landau-like) for very thin scintillator layer or gas detectors. For the P0D the distribution is Gaussian-like because it has about 2 cm of scintillator per plane. The mean energy loss of heavy ($\geq m_\mu$), charged particle in a medium is given by the Bloch-Bethe formula

$$-\frac{dE}{dx} = Kz^2\frac{Z}{A}\frac{1}{\beta^2}\left[\frac{1}{2}\ln\frac{2m_e c^2\beta^2\gamma^2 T_{max}}{I^2} - \beta^2 - \frac{\delta(\beta\gamma)}{2}\right], \tag{5.18}$$

where

- $T_{max} \approx 2m_e c^2\beta^2\gamma^2$ is the maximum energy transfer to an e^- in a collision.
- $K = 4\pi N_A r_e^2 m_e c^2$
- N_A is the Avogadro's number
- r_e the classical electron radius
- I the mean excitation energy
- $\delta(\beta\gamma)$ the density effect correction to ionization energy loss.

For low-energy charged particles, the mean energy loss is proportional to $1/\beta^2$, i.e., inversely proportional to the particle velocity squared, and does not depend on the particle mass. Hence proton and muon of the same kinetic energy have very different mean energy loss; proton loses more energy than muon in the same range. This characteristics of energy loss can be used to distinguish muons from protons. Specifically, the energy deposits in ten scintillator planes from the particle stopping point will be used. Energy deposit in scintillator generates scintillation light and is measured in terms of the number of photoelectrons or light yield. The energy deposit by a charged particle on scintillator plane is given by the total light yield of all track hits on that plane:

$$Q_{\text{plane}} = \sum_{\text{hits}} Q_i. \tag{5.19}$$

It is noted that in addition to the energy loss by excitation of atomic electrons, protons also lose energy from elastic scattering with nucleons in the detector materials. Most of the energy carried off by these nucleons can not be measured since the P0D is not optimized to detect low-energy nucleons. For this reason,

there is more uncertainty in the energy deposit by protons than muons. There are corrections that must be made to this light yield. The first correction is to account for the path length difference in a scintillator layer as the particle with longer path length deposits more energy,

$$Q \rightarrow Q \cos\theta, \tag{5.20}$$

where θ is the angle between the particle direction and the z axis.

The second correction is for the light attenuation along wavelength-shifting fiber. For reconstruction algorithm development, an attenuation curve is used for all bars

$$a(z) = fe^{(-l/c_l)} + (1-f)e^{(-l/c_s)}, \tag{5.21}$$

where $f = 0.77$ is the fraction of the long component, $c_l = 463.4$ cm is attenuation coefficient of the long component, and $c_s = 33.2$ cm the short component. The correction factor for the energy deposit at l away from the sensor is

$$a(l) + a(L-l)\ r\ a(L), \tag{5.22}$$

where L is the length of the fiber and r is the mirror reflectivity. It should be emphasized that the light attenuation correction factor given by (5.21) and (5.22) is different from the one measured from cosmic data. However, this is not incorrect as long as the correction factor in the reconstruction undoes the light attenuation applied in electronics simulation. The light attenuation curve in the electronics simulation will be updated using that measured from cosmic data. In summary, the light yield correction is

$$Q \rightarrow Q_c = Q\cos\theta/(a(l) + a(L-l)\ r\ a(L)). \tag{5.23}$$

The corrected light yield on ten scintillator planes from the stopping point for muons and protons are shown in Fig. 5.4. It is noted that the particle identification is only applicable to 3D tracks since it requires 3D track direction and 3D position at each scintillator plane.

Likelihood classifier

It has been seen that the energy deposit by protons and muons are very different near the stopping point. Since the energy loss is a stochastic process, the energy deposits on different scintillator planes are independent from each other. Therefore, a discriminant constructed from the energy deposit on all scintillator planes is expected to better classify protons and muons. Let us consider the general problem of classifying objects of two classes, ω_1 and ω_2.

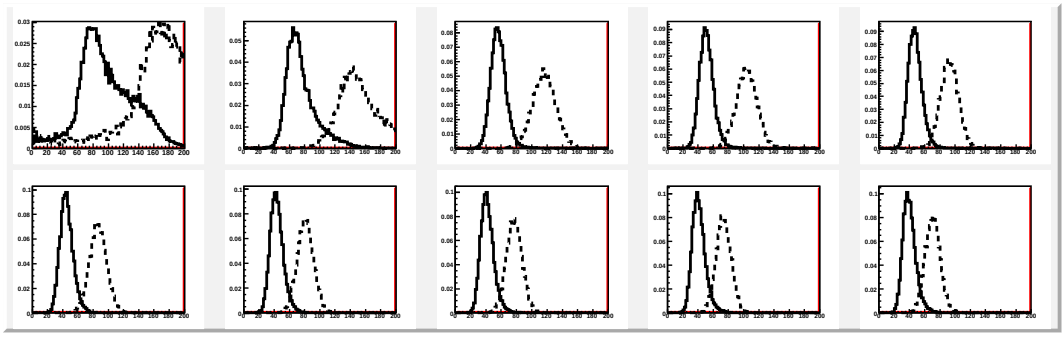

Figure 5.4: Light yield distributions on ten scintillator planes from the stopping point for muons (solid histogram) and protons (dashed histogram) (MC simulation). The x axis is the light yield measured in the unit of photoelectron.

These objects are characterized by a measurable feature vector $\vec{x}$. Let $P(\omega_i|\vec{x})$ be the conditional probability that the object represented by $\vec{x}$ belongs to class ω_i. If the probabilities $P(\omega_1|\vec{x})$ and $P(\omega_2|\vec{x})$ can be determined, then a reasonable decision will be

$$\text{if } P(\omega_1|\vec{x}) > P(\omega_2|\vec{x}) \text{ then } \vec{x} \in \omega_1 \text{ else } \vec{x} \in \omega_2. \tag{5.24}$$

The *posterior probabilities* can be rewritten using Bayes rule:

$$P(\omega_i|\vec{x}) = \frac{p(\vec{x}|\omega_i)P(\omega_i)}{p(\vec{x})}, \tag{5.25}$$

where

$$\sum_{\text{i=1,2}} p(\vec{x}|\omega_i)P(\omega_i) \tag{5.26}$$

is the total probability of $\vec{x}$. The continuous conditional probability $p(\vec{x}|\omega_i)$ is called *likelihood*. Substituting (5.25) into (5.24) and omitting the common denominator, we get

$$\text{if } p(\vec{x}|\omega_1)P(\omega_1) > p(\vec{x}|\omega_2)P(\omega_2) \text{ then } \vec{x} \in \omega_1 \text{ else } \vec{x} \in \omega_2. \tag{5.27}$$

If we want to use only the feature vector $\vec{x}$ to classify objects, i.e., classification using only characteristics of the objects, the prior probabilities $P(\omega_i)$ are set to be the same. In other words, objects of class ω_1 and class ω_2 have the same appearance chance. In this case, the decision becomes

$$\text{if } p(\vec{x}|\omega_1) > p(\vec{x}|\omega_2) \text{ or } \frac{p(\vec{x}|\omega_1)}{p(\vec{x}|\omega_2)} > 1 \text{ then } \vec{x} \in \omega_1 \text{ else } \vec{x} \in \omega_2. \tag{5.28}$$

The ratio in (5.28) is called the *likelihood ratio*, and it can be used to classify objects of class ω_i.

Particle identification using likelihood

We will use the likelihood method to distinguish between protons and muons. The feature vector $\vec{x}$ in this case is the corrected light yield in ten scintillator planes from the stopping point, $\vec{Q}_c$ from (5.23). For tracks traversing more than 10 planes, only the 10 planes near the stopping point are used. For those traversing less than 10 planes, all planes are used. The probability density function (pdfs) of the corrected light yield can be obtained by normalizing the corrected light yield histograms of muons and protons. The likelihood product is

$$\mathcal{L} = \prod_{\mathrm{i}} \frac{p(Q_i|\mathrm{muon})}{p(Q_i|\mathrm{proton})} \tag{5.29}$$

or more frequently used, the log likelihood,

$$\log \mathcal{L} = \sum_{\mathrm{i}} (\log p(Q_i|\mathrm{muon}) - \log p(Q_i|\mathrm{proton})). \tag{5.30}$$

Here the sum is over all scintillator planes traversed by the track.

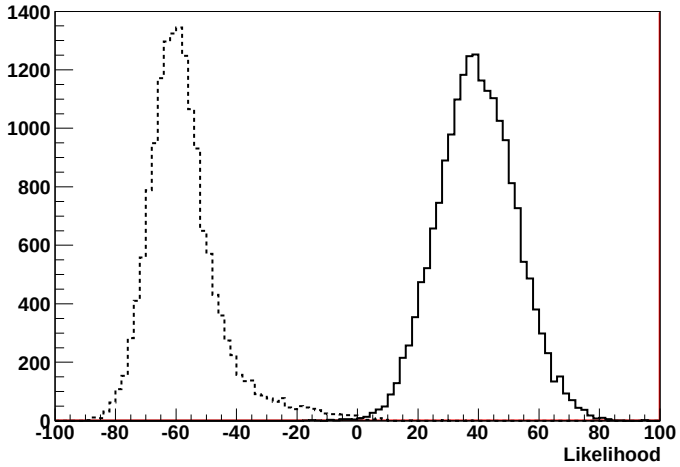

Figure 5.5: Likelihood for protons (dashed histogram) and muons (solid histogram). A vertical line at 0.0 divides the log likelihood into the proton-like and muon-like regions. The region to the left of the divider is proton-like and the one to the right is muon-like.

The first step in using the likelihood method is to make the probability density function for protons and muons. For this purpose, we generate samples of proton of 300 MeV and muon of 200 MeV kinetic energy. The energies of the particles are not important, as long as they stop inside the detector. The second step is to calculate the (log) likelihood distributions for protons and muons. In Fig. 5.5, the log likelihood distributions for protons and muons are shown. The log likelihood for muons is the solid line, and the log likelihood for protons is the dashed line. It is seen that the log likelihood for protons is clearly separated from the log likelihood for muons. A vertical line at 0.0 divides the log likelihood into the proton-like and muon-like regions.

The log likelihood cut has been to used to test classifying protons from muons. We generate MC samples of proton of 200-400 MeV kinetic energy and muon of 100-500 MeV kinetic energy. By using the truth MC, we can tell if a particle is correctly identified. In Fig. 5.6 (left) the momentum of the muon sample is shown, the hatched histogram is the muon which is correctly identified by the log likelihood cut. All the muons in the muon test sample are correctly identified. In Fig. 5.6 (right) the momentum of the proton sample is shown, the unfilled histogram are protons that are correctly identified, and the hatched histogram are protons that are mis-identified as muons.

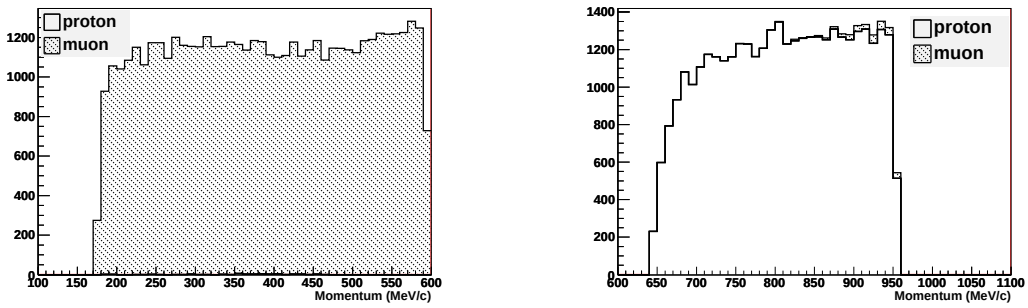

Figure 5.6: True momentum distributions of muons and protons from the particle identification test samples. True momentum distribution of the muon test sample, all muons are correctly identified by the log likelihood cut (hatched histogram) (left). True momentum distribution of the proton test sample, most of the protons are correctly identified (unfilled histogram) with a small fraction misidentified as muons (hatched histogram) (right).

5.4 Muon decay tagging

Charged-current neutrino interactions can also be tagged using stopping muons in the P0D. These stopping muons can either decay or be captured by nuclei through reactions:

$$\mu^- \rightarrow e^- + \nu_\mu + \bar{\nu_e} \tag{5.31}$$

$$\mu^- + p \rightarrow n + \nu_\mu. \tag{5.32}$$

These processes can be detected using the electron from muon decay or the neutron from muon capture. Muon has a lifetime of 2.2 μsec, so it can make delayed hits in the detector. Typical timing for hits from other particles is about 100 ns (see Fig. 5.7). The energy spectrum of electron from muon decays is shown in Fig. 5.7, the cutoff threshold is given by $m_\mu/2$. It is seen that most electrons from muon decay are at low energy. The range of electrons at this energy is about 15 cm. This range is significantly reduced if the electrons traverse the lead radiators. Therefore, hits produced by the decay electron are connected to those from the parent muon and are within about 15 cm of the stopping point. In the following, we will describe the algorithm to search for hits from muon decay.

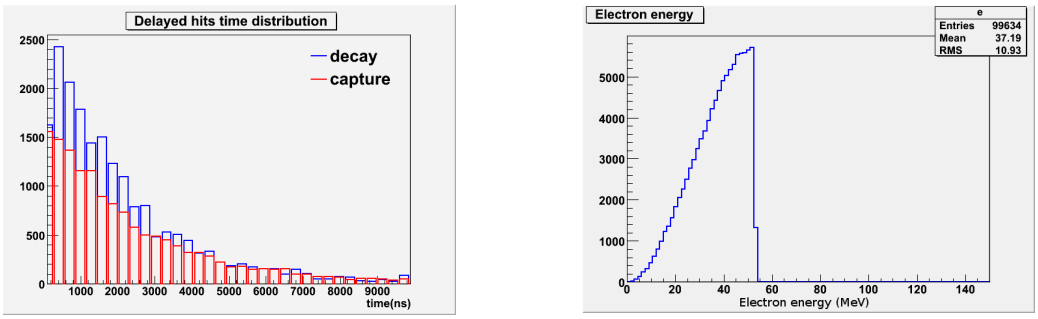

Figure 5.7: Time distribution of hits from muon decays and captures, gaps between bins are Trip-T reset periods, the plot is generated using 4000 decays and captures each (left) and energy spectrum of electron from muon decay (right).

The search for hits from the stopping muons are carried out independently in xz and yz planes. In the following, we describe the algorithm for one projection plane. The hits in a each event are divided into two groups: hits in the current bunch and *delayed hits* which consists of hits in the later bunches and those from the after-spill period. Remember that the Trip-t integration time of all 23 timeslices is longer than the spill length. First hits in the current

bunch are clustered using the density-based clustering algorithm. If there is no cluster which has at least five hits, the search is stopped since there are not enough connected hits to reconstruct a neutrino interaction and hence there is no need to find the stopping muon. If there are clusters, then the hits in the current bunch and the delayed hits are overlapped in time and the hits which belong to the largest cluster are used as a seed to expand the cluster into the delayed hits. This expansion is a form of clustering and again the density-based clustering is used. The delayed hits that are added to the cluster during the expansion are considered candidate hits from the muon decay. These candidate hits are further required to be time- and space-connected. The requirement is that a decay hit has at least one decay hit within 20 ns in time and 5 cm in space. The candidate hits satisfying these requirements are accepted as hits from the muon decay. Finally, the decay hits which have been found are removed from the delayed hits, and the muon decay tagging is repeated for the next bunch in the event. Strictly speaking, there could be more than one neutrino interaction in the same bunch but it is unlikely. In that case, the muon decay tagging should move to the next neutrino interaction in the same bunch.

The muon decay tagging algorithm described above has been tested using a sample of Monte Carlo simulated stopping muons. The muon sample has a flat energy distribution from 50 MeV to 100 MeV and a uniform angular distribution. The muon energy range is to ensure that parent muons produce enough hits to trigger the muon decay search and stop inside the detector. The muon vertex is uniformly distributed in the water target region. The muon vertex time is uniformly distributed in the 15 bunches, each of 241 ns. By looking at the other particles produced at the stopping point using MC truth, it is found that about 30% of muons in the sample are captured by nucleus, and about 70% decay. The muon decay tagging is run on this sample and the tagging efficiency is about 50%. This efficiency also includes the number of muon captures which are detected by the algorithm. It is noted that this efficiency is for the spill structure of 15 bunches, each of 241 ns. The tagging inefficiency is caused by the electron stopping in water or lead radiator, the neutron escaping the detector without any interactions, and the electronics dead time.

5.5 Track extrapolation from the TPC

The TPC is located downstream of the P0D detector. Since it has better particle tracking and identification capabilities, charged particle tracks found

by the TPC are extrapolated into the P0D. The extrapolation enables the detection of charged particle tracks that are too short to be detected by the P0D itself or obscured by showers. The extrapolation algorithm is described below.

Charged particle tracks from the TPC are filtered to select only tracks that appear to come from neutrino interactions in the P0D. This is done by requiring the most upstream track point to be inside an area of 1.8m$\times$ 1.8m centered around the z axis. Each of these selected tracks is then extrapolated into the P0D. The extrapolation is implemented in terms of the discrete Kalman filter. Similar to the track fitting, the dynamic model for the filter is a straight trajectory with small random perturbation to the particle direction. For each track, the extrapolation proceeds in the following steps. First the filter is initialized with the position and the reversed direction of the most upstream track point and their corresponding covariances. The direction is reversed because the track is going forward in the beam direction while the extrapolation is backward. Next the prediction step of the filter is used to project the track point to most downstream scintillator plane of the P0D. If there are no hits in a window of 4 cm around the projected point, the extrapolation is stopped. If there are hits, then the energy-weighted position of these hits is calculated. Remember that the same weighting was done for hits in the same scintillator plane before the track fitting. The equation is reproduced here:

$$\bar{x} = \sum_{\text{hits}} q_i x_i, \tag{5.33}$$

where the sum is over all hits in the window, and q_i is the fractional energy, and x_i is the position. Finally, the update step of the Kalman filter uses the energy-weighted position (5.33) to update its state and covariance. Now the updated state and the covariance can be used in the prediction step to project to the next plane. These steps are repeated until the filter reaches the front of the P0D or the extrapolation fails because of empty hits in the window. Note that the extrapolation alternates between the xz and yz planes. At the x plane, the y position is not updated, and vice versa. At the end of a successful extrapolation, i.e., no track loss, a three-dimensional track is found in the P0D. Since the particle corresponding to the extrapolated track escapes the detector, the P0D particle identification which is applicable to stopping particle track would not be efficient. Therefore, the particle likelihood of the extrapolated track is copied from the original TPC track.

5.6 π^0 reconstruction

The π^0 is reconstructed using the hits which are not associated with charged particle tracks. The following variables of the π^0 are required for analysis:

- Interaction vertex
- Momentum
- Invariant mass

The interaction vertex and invariant mass could be used to select good π^0 sample. The reconstruction of π^0 from neutral current neutrino interactions are in general complicated because of the contaminating hits from other particles. Let us consider the simpler case of π^0 from a particle gun where all the hits are produced by the π^0.

5.6.1 Particle gun π^0 reconstruction

For simplicity, let us further assume that π^0 only decays into two γs. The Dalitz decay mode, $\pi^0 \rightarrow e^+e^-\gamma$, has the branching ratio of less than 2%. In principle, the reconstruction of π^0 involves the reconstruction of the two daughter γs. The π^0 energy momentum is simply the sum of the γ energy momenta. The vertex can be extrapolated from the γ directions. The invariant mass can also be reconstructed from the energies of the two γs and the open angle

$$m^2_{\pi^0} = 2E_1E_2(1 - \cos\theta), \tag{5.34}$$

where E_1, E_2 are the energies of γ_1, γ_2, respectively, and θ is the open angle between the two γs. The invariant mass is a powerful variable to separate the π^0 from the backgrounds. However, the reconstruction of the two γs presents a challenging data association problem, especially in a target geometry detector where it is instrumented to measure forward-going particles. Although for π^0 from neutral current interactions the total momentum of the two γs is in the forward direction, the momentum of individual γ is arbitrary. The high-angle γs could make isolated showers since they transverse fewer radiator layers and hence it is hard to associate which shower to which γ. In addition, low-energy γs produce so few hits that it is difficult to determine the γ direction from the shape of the hit pattern. Finally, γ showers in xz and yz projection planes must be matched to form 3D showers. Therefore, we propose an approximate

method to reconstruct π^0 without having to solve the data association problem. The momentum of each γ can be approximately reconstructed

$$\vec{p}_\gamma = k \sum_{\gamma \text{ hits}} \hat{r}_i Q_i, \tag{5.35}$$

where $\hat{r}_i$ is the direction vector from the γ vertex, Q_i is the hit light yield after light attenuation correction, and k is the energy calibration constant. Let us find the error involved in the approximation (5.35). When the direction vector of all the hits are collinear, the direction vectors can be taken out of the sum and the momentum is simply

$$\vec{p}_\gamma = \hat{r} k \sum_{\gamma \text{ hits}} Q_i = \hat{r} E_\gamma \tag{5.36}$$

where $\hat{r}$ is the γ direction vector. Equation (5.36) is the exact relativistic relation between the γ energy and momentum. Note that the direction vector in (5.35) can be decomposed into the transverse and longitudinal components with respect to the γ direction, $\hat{r}_i = \hat{r}_{i\parallel} + \hat{r}_{i\perp}$, then (5.35) can be rewritten:

$$\begin{aligned} \vec{p}_\gamma = k \sum_{\gamma \text{ hits}} (\hat{r}_{i\parallel} + \hat{r}_{i\perp}) Q_i = \hat{r} E_\gamma + k \sum_{\gamma \text{ hits}} \hat{r}_{i\perp} Q_i \\ \rightarrow \vec{p}_\gamma - \hat{r} E_\gamma = k \sum_{\gamma \text{ hits}} \hat{r}_{i\perp} Q_i, \end{aligned} \tag{5.37}$$

where we have substituted (5.36) for the longitudinal term. From (5.37), it is clear that the error of the approximation is given by the transverse term. In other words, the approximation assumes that the transverse component of the direction vector is negligible. This is especially true for γ showering far from the vertex.

The π^0 momentum is simply the total momenta of the two γs.

$$\vec{p}_{\pi^0} = k \sum_{\gamma_1 \text{ hits}} \hat{r}_i Q_i + k \sum_{\gamma_2 \text{ hits}} \hat{r}_i Q_i = k \sum_{\pi^0 \text{ hits}} \hat{r}_i Q_i \tag{5.38}$$

This equation allows calculating of the π^0 momentum without having to separate the gamma hits, the error introduced by this method is given by (5.37). In Fig. 5.8 (left) the relative deviation of the reconstructed momentum from the true momentum is shown. The mean shift due to the approximation is less than 1.5%. A MC sample of π^0 with a uniform energy distribution with the range from 50 MeV to 400 MeV and forward direction is used to obtain the

plot. The light yield Q_i is corrected for light attenuation using the true hit position from MC and also the true vertex is used to calculate the direction vector $\hat{r}_i$.

Similarly, the π^0 energy can also be reconstructed

$$E_{\pi^0} = k \sum_{\pi^0 \text{ hits}} Q_i. \tag{5.39}$$

Now given both the momentum and energy, the invariant mass can be calculated

$$m_{\pi^0} = \sqrt{E_{\pi^0}^2 - p_{\pi^0}^2}. \tag{5.40}$$

In Fig. 5.8 (right) the invariant mass calculated using this equation is shown. The calibration constant k is determined so that the mean of the relative deviation of the reconstructed energy is zero. It should be emphasized that for real neutrino data, the calibration constant k must be determined from the absolute energy calibration. This energy calibration could be done by using the π^0 invariant mass of a well-reconstructed π^0 sample from charged current interactions. The calibration constant k is then obtained by minimizing the quantity

$$\left(m_{\pi^0} - k\sqrt{2Q_1Q_2(1-\cos\theta)}\right)^2, \tag{5.41}$$

where $m_{\pi^0} = 134.97$ MeV/c^2 and Q_1, Q_2 are the light yield produced by the two γ's.

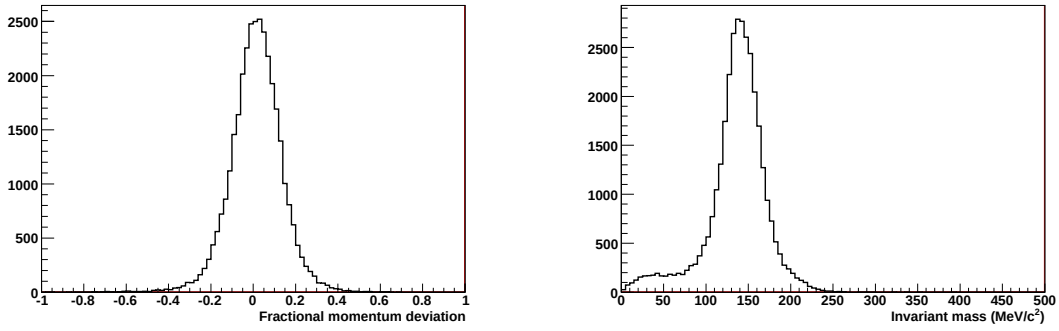

Figure 5.8: The relative deviation of the reconstructed momentum from the true momentum, the mean shift due to the approximation is less than 1.5%. (left). The π^0 invariant mass calculated using the approximate momentum (5.40) (right) (MC simulation).

The momentum reconstruction requires the π^0 vertex, it can be estimated by using a grid search. The search scans the whole detector to find the ver-

tex position which maximizes the (log) likelihood function of these likelihood variables:

- The ratio of energy in clusters to the total energy.
- The number of clusters
- Cluster width
- The distance from the vertex to the closest cluster.

Here the width of the cluster is expected to be of the order of the Moliere radius and the distance from the candidate vertex to the closest cluster is about the mean free path which is 9/7 of the effective radiation length. Note that this grid search is very computing extensive, a new vertex finder has been developed which searches for the vertex around the principal axis determined by a PCA analysis of all π^0 hits.

5.6.2 Neutrino interaction π^0 reconstruction

For neutrino data, the π^0 reconstruction is more difficult since there are contaminating hits from other particles, especially from protons and neutrons. After charged particle reconstruction, the hits associated with charged particle tracks are removed, then the remaining hits are passed to the π^0 reconstruction. The momentum and energy are reconstructed similarly the particle gun π^0 using (5.35) and (5.39), from which the invariant mass (5.40) can be calculated. It is noted that for π^0 produced by the reaction

$$\nu_\mu + p \rightarrow \nu_\mu + p + \pi^0, \tag{5.42}$$

the vertex can be better reconstructed using the proton track. For other π^0 production channels, the grid search described above is used. In general there is more uncertainty in the momentum and energy for neutrino data since there are contaminating hits from other particles from the neutrino interaction vertex.

5.7 Application on neutrino MC

In previous sections we have described the event reconstruction and showed tests for various algorithms using single particle MC. In this section we will apply the event reconstruction on neutrino interaction MC.

5.7.1 Neutrino MC

Neutrino MC data are generated using the NEUT event generator[45]. The NEUT generator uses the T2K neutrino spectrum and simulates the interactions of neutrino on oxygen nucleus. Currently (2008), the NEUT generator does not used any flux information from beam simulation. The final-state particles from neutrino interactions are tracked inside the nuclear medium and various processes such as inelastic scattering, charge exchange, absorption are taken into account. The kinematics of the particles from neutrino interactions that leave the nucleus are saved for use in detector simulation. Note that not all the particles at the neutrino interaction vertex leave the nucleus. Particles like π^0 could decay inside the nucleus or π^+ could charge exchanges into a π^0.

Kinematics from the event generator are passed to the detector simulation which is based on GEANT4. The event generator and detector simulation are independent, the intermediate results are saved on disk. The detector simulation simulates the interactions of particles with detector materials, bends charged particle trajectories in the magnetic field. The neutrino interaction vertices are distributed throughout the detector using the mass density weighting. The detector simulation steps each particle through the detector, applicable interactions are invoked along the path length. By default, the step length depends on the traversing detector materials and the amount of energy loss. This step length can be set manually, for example, to test track fitting algorithm a small step length of 1 mm is used to easily to compare the true trajectory points and the fitted track points. Energy deposit from charged particles in the sensitive volume are collected and associated with the corresponding scintillator bar. It should be noted that during the detector simulation, secondary particles from final-state particles and their kinematics are also saved. For example, given a π^0 in the detector, it is possible to trace the parent of the π^0.

The amount of energy deposit in scintillator bar is converted to the number of photons using the electronics simulation. The conversion factor is such that the output light yield matches that from the light yield measurement using cosmic muons. The electronics simulation also applies light attenuation to the number of photons using the true distance to the photosensor. It also rejects hits that fall in the electronics dead time, i.e., the reset time between two consecutive Trip-t integration periods. The output of the electronics simulation has the same format as the real data.

For this study, 10^5 neutrino interactions from the NEUT generator are used. At full power of the J-PARC accelerator, the number of neutrino interactions in the P0D is estimated to be about 1.7 per spill. For simplicity, one neutrino

interaction per spill is assumed.

5.7.2 MC processing and reduction

Neutrino MC data are passed to the event reconstruction. The parameters of the timing structure for the reconstruction must match those of the MC. This is important, especially to have a more realistic muon decay tagging. The reconstruction saves a lot of redundant information since it is the most time consuming step. The output of the reconstruction is further distilled, only variables needed to do physics analysis are written to a lightweight data summary tree (DST).

5.7.3 Event selection

The signal events in the P0D are single π^0 from neutral current interactions. These include the π^0 from the following reaction channels:

$$\nu_\mu + N \rightarrow \nu_\mu + N + \pi^0 \tag{5.43}$$

$$\nu_\mu + {}^{16}O \rightarrow \nu_\mu + {}^{16}O + \pi^0, \tag{5.44}$$

where N is either p or n. Because of the interactions of final-state particles, the number of single π^0 escaping the nucleus is not the same as that at the neutrino interaction vertex. The number of signal events are defined as the number of events with a single π^0 leaving the nucleus. There is a small fraction of secondary π^0 produced by nucleons in the detector.

Background events are any electromagnetic showers that do not come from the signal events. The electromagnetic showers could come from charged current single π^0 production, multi-pion and in-elastic interactions. The neutral current backgrounds include the neutral current multi-pion, in-elastic interactions, and quasi-elastic interactions on nucleons. The charged current backgrounds can be largely removed by tagging the muon using tracks with muon-like particle identification or muon decay. The neutral current and charged current can be further reduced by using the characteristics of electromagnetic showers from π^0 decays. Specifically, except for the Dalitz decay mode, $\pi^0 \rightarrow \gamma e^+ e^-$, π^0 decays into two γ's which is expected to produce 4 showers on the 2D projection planes. However, because of the long effective radiation length ($\sim$ 30 cm) in the water target, the two γ's do not always shower or one gamma could make two separate showers. The following criteria are used to select π^0:

- No 3D tracks with muon-like likelihood.

- No 2D unmatched tracks longer than 40 cm.
- No μ^- decay.
- Number of 2D showers from 3 to 5.
- 80 MeV/c^2 $\leq m_{\gamma\gamma} \leq$ 190 MeV/c^2.
- Reconstructed vertex inside the fiducial volume. The fiducial volume is defined as the volume inside $\pm$6 cm along the z direction and $\pm$25 cm along the x, y direction from the edge of the detector.

The first three cuts are to remove the charged current backgrounds. The next two cuts select π^0 using its shower characteristics. In Table. 5.7.3, the number of signal events and charged current backgrounds after each cut are shown. The final reconstruction efficiency for saved π^0 in the fiducial volume is 18.5% and the μ^- rejection efficiency is 99.7%.

Table 5.1: Number of signal and charged current background events after each cut.

Selection cuts	NC1π^0	μ^-
All	1228	65778
No muon-like track	1182	29644
No unmatched track	1133	22340
No μ^- decay	1037	14059
Number of showers	572	3713
Invariant mass	294	1203
Fiducial volume	223	180

5.7.4 Final π^0 sample

There are 501 events that passed all the π^0 selection cuts. Using the truth information, the signal and background events can be distinguished. There are 223 signal events and 278 background events. The π^0 purity in the final sample is 44.5%. The π^0 reconstructed energy is shown in Fig. 5.9. The background events are separately shown for charged current (35.9%) and neutral current backgrounds (19.5%).

The backgrounds can be further broken into individual reaction modes (Table 5.7.4). The dominant charged current background is caused by the

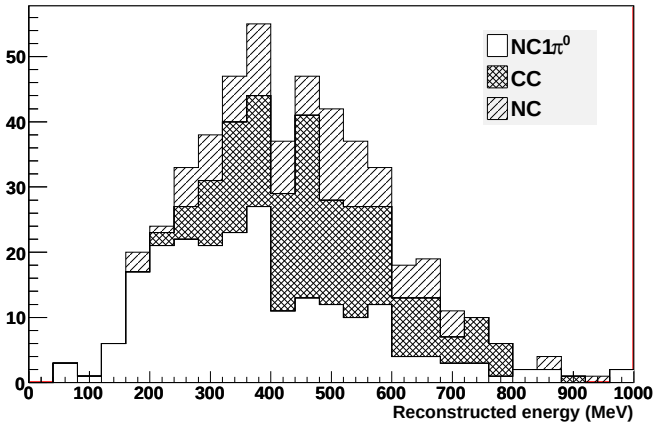

Figure 5.9: Reconstructed energy of the final π^0 sample. The contributions from the signal (unfilled) and the backgrounds (hatched) are shown separately.

charged current quasi-elastic scattering (CCQE). This is mostly because the reconstruction could not identify the hit pattern and the large cross section of this interaction mode. The backgrounds by the charged current multiple pion production and in-elastic scattering (CC$n\pi$) are smaller since their cross sections are small at low energy and most of the events produce many hits, and therefore, are removed by the cut on the number of showers. The neutral current background is dominated by the multiple pion events (NC$n\pi$), these events usually have one or more π^0. The single π^0 background accounts for 28% of the neutral current background. Actually these are not background events, but they are single π^0 from outside the fiducial volume. This background will be removed by a better π^0 vertex reconstruction.

The position of muons from charged current backgrounds are shown in Fig. 5.10. Of the muons near the edges, those escape the detector can be further detected using the P0DECAL, which surrounds the P0D, or the SMRD.

Table 5.2: Number of charged current and neutral current background events from different reaction modes.

Reactions	events	percentage(%)
CCQE	77	42.7
CC1$\pi^{\pm}$	46	25.5
CC1π^{0}	45	25.0
CCnπ	12	6.7
NCQE	15	15.3
NC1$\pi^{\pm}$	21	21.4
NC1π^{0}	28	28.5
NCnπ	34	34.6

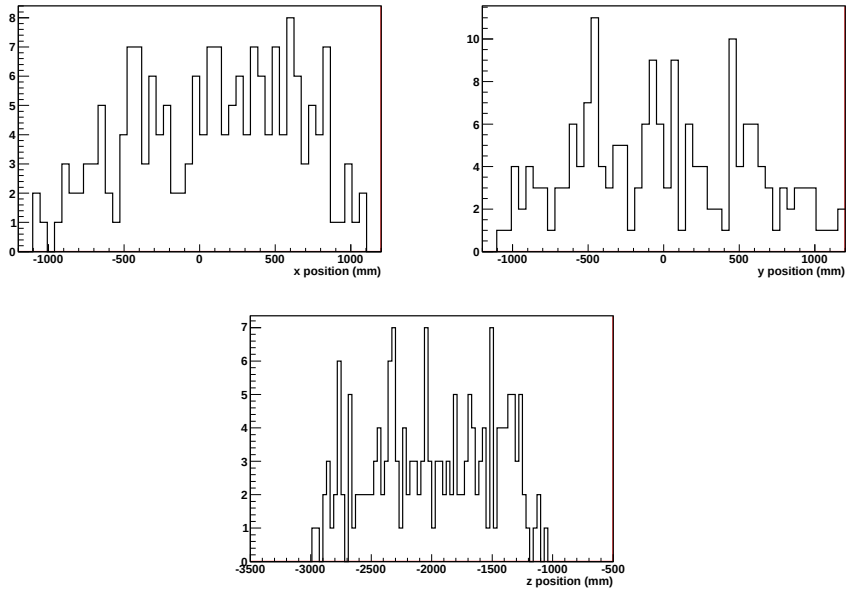

Figure 5.10: Position of muons from charged current backgrounds.

Chapter 6

Energy calibration of the P0D using cosmic ray muons

6.1 Introduction

The cosmic ray tests were done separately for individual SuperP0Dules before their installation into the final position. These tests are used for hardware and software validation. On the hardware side, the cosmic ray tests make sure that all the channels are connected and working properly. The full readout chain from the scintillator bars to the data acquisition computer can be checked. On the software side, from the low-level software (firmware) to event reconstruction can be debugged using these tests.

The cosmic muons can also be used for energy calibration of the detector. Cosmic muons are minimum ionizing particles (MIP). This means that the energy losses along their path lengths are almost constant, independent of the their initial energy. This source of energy is used for calibrating by requiring that the mean energy deposit per unit path length for all detector channels are the same. By taking the cosmic data at different running conditions (temperature, photosensor bias voltage), the performance of the photosensors can be studied. Finally, light attenuation along WLS fibers can be measured by comparing the energy deposits at different distances from the photosensor.

In this chapter, we will present the procedure to correct for gain change, the measurement of light attenuation for all the channels, and the energy calibration.

6.2 Data summary

This chapter presents the analysis of cosmic data from the P0D upstream ECAL. The data from the water target and central ECAL modules has been

quality checked and made sure that the cosmic trigger works properly, but has not been analyzed. There are total of 215 cosmic runs, numbered from 1450 to 1915, each run has an hour of cosmic data at around 30 Hz trigger rate. Each cosmic run is preceded by a two-minute pedestal run which is used for calibration. The pedestal runs are actually cosmic runs with the zero suppression turned off. The ambient temperature and humidity were recorded every 30 seconds by a sensor mounted on the top of the MPPC side. The temperature data is read out independently from the cosmic data stream by a USB cable connected to the DAQ computer. The MPPCs were biased at 70.9 V, and applied the fine voltage offsets from Hamamatsu. Fig. 6.1 (left) shows the temperature variation during the cosmic runs, up to run 1779. It can be seen that the temperature variation is about 6^0C from 25^0C to 31^0C. This large temperature variation was caused by the AC being turned off at night. It should be mentioned that the sensor measured the temperature at one particular location and there was no information regarding the temperature uniformity throughout the detector. The temperature variation during each cosmic run can also be monitored. For each cosmic run, the difference ΔT between the minimum and maximum temperature is used to characterize the temperature variation during the run. Fig. 6.1 (right) shows the maximum temperature variation during each cosmic run ΔT versus run number.

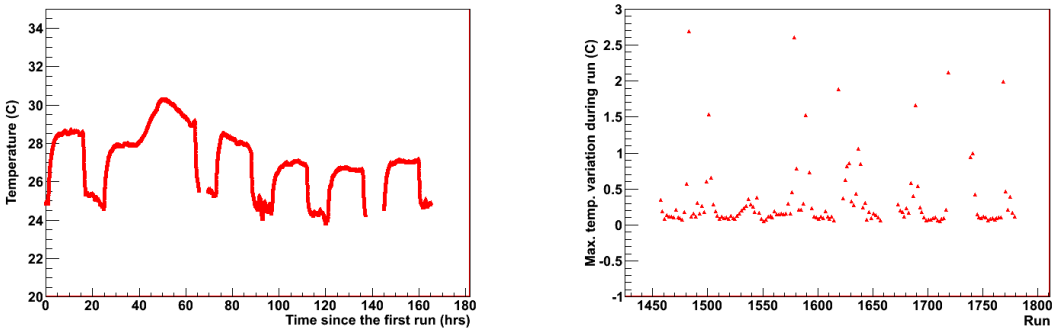

Figure 6.1: Temperature variation during cosmic runs (left) and maximum temperature variation during each cosmic run versus run number.

6.3 Charge calibration

6.3.1 ADC spectrum fitting and gain

The high-gain ADC spectrum for one channel from a pedestal run is shown in Fig. 6.2. The dominant peak is the pedestal which consists of empty events, i.e., events with no output from the MPPC. The smaller peak to the right of the pedestal peak is the dark noise one (equivalent) photoelectron peak. A small fraction of events above 1.5 p.e. is also visible. The position of the two peaks can be determined by fitting the ADC spectrum to a double Gaussian function. At high gain when the two peaks are well separated, fitting the individual peaks to a Gaussian function is also possible. The double Gaussian fitted curve (solid line) and two independent Gaussian fitted curves (dashed) are shown in Fig. 6.2. The pedestals obtained from fitting the ADC spectra all of channels on a TFB board is shown in Fig. 6.2 (right).

The difference between the one p.e. and pedestal peak is conveniently defined as the gain

$$G = 1\text{pe} - \text{pedestal}. \tag{6.1}$$

The gain defined this way is related to the conventional gain by a constant k/e, where k is the ADC resolution and e is the electron charge.

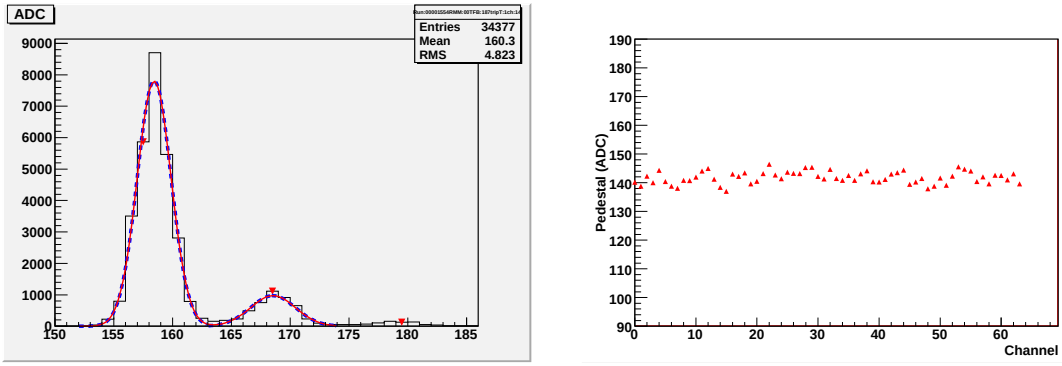

Figure 6.2: High-gain ADC spectrum for one channel (solid histogram) with a double Gaussian fit (solid curve) and two independent Gaussian fits (dashed curve). Pedestal distribution for one TFB board (right).

6.3.2 MPPC noise characteristics

There are two kinds of noise inherent to the MPPCs: random dark noise caused by thermal electrons and noise which correlates with signals.

Dark noise

The dark noise is caused by electrons thermally excited in the depletion region of the photosensor and produces one equivalent photoelectron due to the high gain. The dark noise is characterized by the dark noise rate. The dark noise rate can be measured using the high-gain ADC spectrum taken from the pedestal runs. The number of empty events is defined as the area under the fitted Gaussian curve and within $\pm 3\sigma$ from the pedestal peak. The number of dark noise events is the difference between the total events and the empty events. It is noted that the area under the one photoelectron peak is not the number of dark noise events since dark noise events can create more than one photoelectron due to the correlated noise. The dark noise rate is calculated by dividing the fraction of dark noise events by the Trip-t integration period of 250 ns. In Fig. 6.3, the mean dark noise rate over all the channels versus the temperature and gain are shown separately for X and Y bars. It can be seen that the mean dark noise rate is around 650 KHz and the spread is about 100 KHz. From the plot on the right, the dark noise rate is relatively constant from 9 to 12 ADC counts. This can be qualitatively explained by the fact that the dark noise depends on two competing factors: the number of thermally excited electrons in the depletion region which increases exponentially with the temperature and the over-voltage which decreases with increasing temperature.

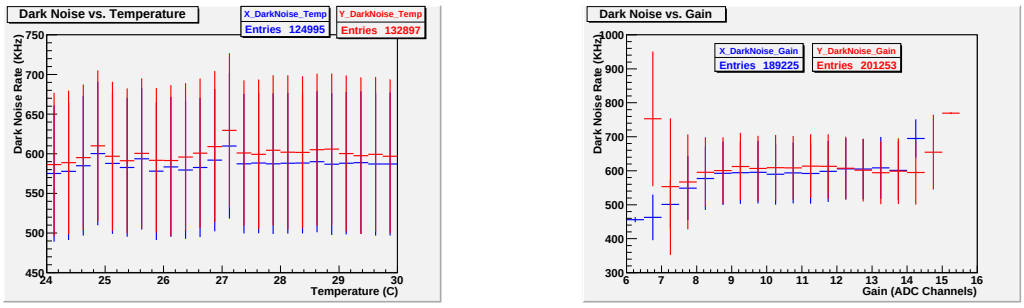

Figure 6.3: Dark noise versus temperature (left) and dark noise versus gain (right) .

Correlated noise (crosstalk, afterpulsing)

The second type is correlated noise, i.e., additional avalanches triggered by existing avalanches previously generated by signal or dark noise. For example, an afterpulsing avalanche sometimes occurs after the original avalanche in the same pixel. It is believed to be triggered by a charge carrier that was produced

by the original avalanche and trapped on an impurity. Crosstalk happens when a firing pixel causes neighboring pixels to fire. In contrast to the dark noise which is random and independent of the size of the signal, the correlated noise scales with the signal. The average number of secondary avalanches caused by an original avalanche either through afterpulsing or crosstalk is called the correlated noise probability. This probability can be measured from the pedestal runs. Remember that the number of zero events can be accurately determined by fitting the pedestal peak to a Gaussian function. Assuming that the dark noise process is random and hence the number of occurrences of dark noise events obeys Poisson statistics, then the number of 1 p.e. events can be predicted from the number of zero events

$$\lambda = -\ln P(0) \tag{6.2}$$

$$\rightarrow \quad N_{\text{pred.}} = \lambda e^{-\lambda} \tag{6.3}$$

where $P(0)$ is the probability of zero events and λ is the Poisson parameter. The number of measured 1 p.e. events $N_{\text{expt.}}$ is given by the area under the 1 p.e. fitted Gaussian curve and within $\pm 3\sigma$ from the peak. The events that are missing from the predicted 1 p.e. events are considered to have caused correlated noise. The correlated noise probability is defined as

$$\text{c} \equiv \frac{N_{\text{pred.}} - N_{\text{expt.}}}{N_{\text{pred.}}} \tag{6.4}$$

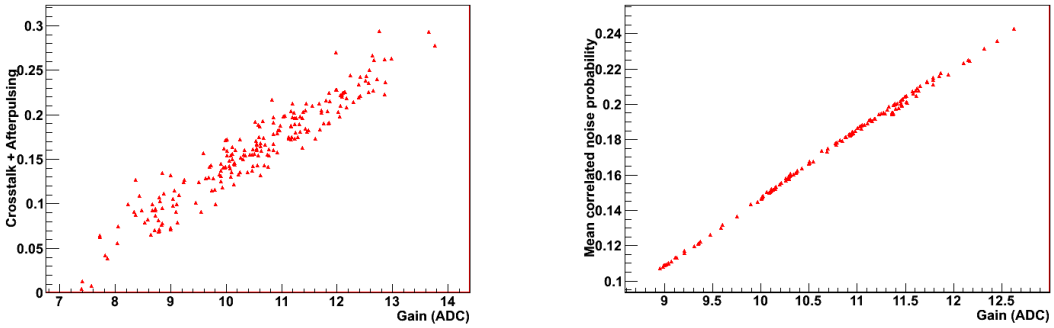

Figure 6.4: The correlated noise probability versus gain for one channel and the mean correlated noise probability over all the channels versus gain.

The correlated noise probability is calculated for all the channels for all runs using pedestal data. The correlated noise probability for one channel is shown in Fig. 6.4. The correlated noise strongly correlates with the gain. This

is because the higher the gain, which means higher overvoltage, the more likely that secondary avalanches are produced by an original avalanche. In Fig. 6.4, the mean correlated noise probability over all channels as a function of the gain is shown. The mean correlated noise probability at the nominal gain of 10 ADC counts is about 15%.

Photon Detection Efficiency The photon detection efficiency is defined as the fraction of detected photons over the incident photons. It depends on three factors:

- Quantum efficiency
- Geometric factor
- Avalanche probability

The quantum efficiency depends on the properties of the semiconductors from which the sensor is made. For the same sensitive area, the geometric factor depends on the number of pixels. The more pixels create more inactive area between the pixels and hence smaller geometric factor. The avalanche probability is dependent on the bias voltage; high bias voltage increases the avalanche probability. The PDE for green light has been measured and found to be greater than 25%. The PDE as a function of the over-voltage also has been measured[43]

6.3.3 TFB calibration using charge injection

The TFB response is not a simple linear function, but instead exhibits an approximately bi-linear behavior, i.e., it is only linear only in the regions below and above certain value of input charge, and there is a nonlinear transition between the two regions. The response varies from channel to channel. Therefore, the response function of every channel on the TFB must be measured using the onboard charge injection circuit. This is done by measuring the digitized charge output from the TFBs for a range of charge input. The result is a relating function between the digitized charge output measured in the unit of ADC counts and the amount of injected charge. The inverse function is used to translate the digitized charge output into charge input.

Charge is injected by the onboard circuit to every four channels per Trip-t, e.g., 0-4-8-12 and into the Trip-t second integration cycle. For each charge injection level which corresponds to a fixed amount of charge, data is taken for 30 seconds collecting about 800-900 events. After looping over all the 90

levels, the data is taken for the next four channels on the Trip-t. The charge injection data are taken with the MPPC bias set above the breakdown voltage. Therefore, for the high-gain channel, the ADC spectrum is similar to that of the pedestal runs which has the pedestal peak and one p.e. peak. For the low-gain channel, the ADC spectrum has a single pedestal peak, and the dark noise peak falls into the pedestal peak because of the low gain. The effect of the charge injection is to move both the pedestal and the 1 p.e. peaks to higher ADC value while keeping the gain unchanged. This is resulted from the fact that dark noise charge from the MPPC is added on top of the injected charge. For this reason, the pedestal peak is referred as 0pe peak from now on in this section.

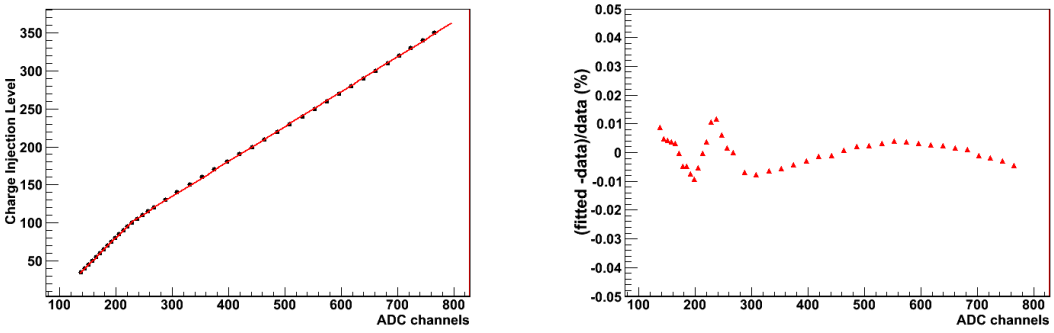

Figure 6.5: TFB inverse response function: charge injection level versus ADC counts (circle) and the bilinear fitted curve (left). Residuals of the bilinear fit versus ADC counts (right).

For high-gain ADC spectra, both the 0pe and 1pe peaks are found in the same way as described for the pedestal runs. For low-gain ADC spectra, the 0pe is estimated first, then it is fitted to an asymmetric Gaussian. The asymmetric Gaussian fits better to the low-gain ADC spectra since the upper side of the pedestal peak gets contributions from dark noise events. These fits are done for the ADC spectra from all channels and charge injection levels. After the fitting to obtain the position of the 0pe peak for all charge injection levels, for each channel there is a set of data points which represent the response of the TFB for this channel (show figure for both low gain and high gain ADC). These data points will be used to correct for TFB response in data calibration. For this purpose, it has to be parameterized to be stored and accessed efficiently in the calibration database. The simplest way to parameterize is to use a bi-linear function. This function has four parameters, the two slopes for

two regions, the intercept, and the kink where the slopes change.

$$Q(x) = \begin{cases} k_1 * x + (k_2 - k_1) * \text{kink} + b_2 & \text{if x} \leq \text{kink} \\ k_2 * x + b_2 & \text{if x} > \text{kink} \end{cases} \tag{6.5}$$

where x is the digitized charge measured in the units of ADC counts. Fig. 6.6 shows the data of the injected charge versus ADC counts for the high-gain channel and the fitted bi-linear line. The plot on the right shows the relative residuals of the fit. It can be seen that the residuals are less than 0.01 or 1%.

Using the charage injection data, the linearity of the number of (equivalent) photoelectrons versus the input charge in the full dynamic range can be studied. In other words, it is used to check after correcting for TFB response if the number of photoelectrons is a linear function of the input charge. The amount of charge corresponding to an ADC value can be obtained using the fitted bilinear functions. Below 800 high-gain ADC count, the high-gain channel is used while above the threshold the high-gain becomes saturated and the low-gain channel is used. The amount of charge corresponding to one photoelectron can be calculated from the 1pe peak

$$Q_{1pe} = k_1 * (1pe - 0pe), \tag{6.6}$$

where k_1 is the slope of the high-gain channel defined in (6.5). Fig. 6.6 shows the number of photoelectrons versus input charge for the whole dynamic range (triangle) and the fitted line. The dashed vertical line indicates the fitting range. The plot on the right shows the relative residuals of the fit. It can be seen that the relative residuals are less than 5%.

The parameterization of the TFB response function using the bilinear function is simple and the fit to this function is robust. This parameterization results in the relative residuals to be within 5%. Higher-order polynomials and even spline function have been tried to parameterize the response function. Although the relative residuals could become smaller, the fit to these functions is less stable. Especially, it is hard to store the splines for all the channels in a database.

6.3.4 One photoelectron calibration

Charge output from individual pixels on a MPPC are summed to a single pulse. The pulse size is proportional to the number of firing pixels. For a fixed number of incident photons, the higher the gain (higher over-voltage), the larger the pulse size. In the absence of the correlated noise, the number of measured photons should remain unchanged, independent of the gain. This

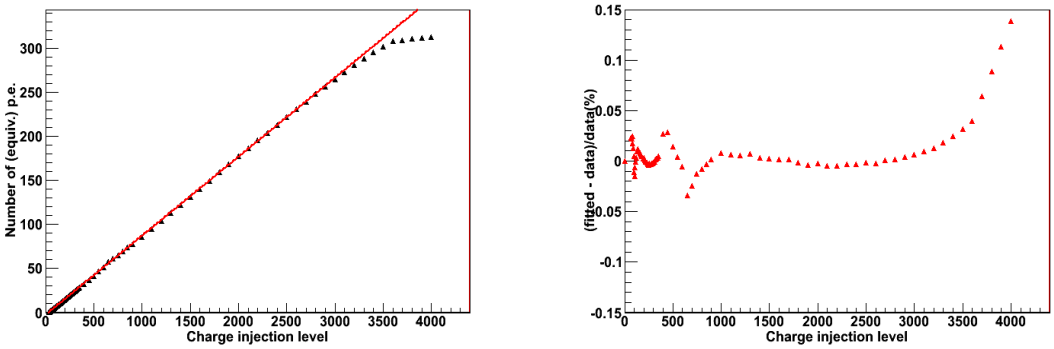

Figure 6.6: The number of (equivalent) photoelectrons versus charge injection number for the whole TFB dynamic range (triangle) and fitted line (solid) (left). The fitting range is from 0 to 3000 charge injection levels. The residual of the fit (right).

can be done by the one photoelectron calibration. When the gain increases, the pulse size becomes larger, however, the one photoelectron pulse size also becomes larger. Therefore, this will cancel the increase in the signal pulse size. The number of photoelectrons corresponding to an ADC value is

$$N_\gamma = \frac{Q(ADC) - Q(0pe)}{Q_{1pe}}, \tag{6.7}$$

where $Q(x)$ is defined by (6.5) and Q_{1pe} is given by (6.6). The numerator is the charge after corrected for TFB response.

6.4 Muon track reconstruction and selection

After charge calibration, the calibrated data are saved on disk for further analysis. In calibrated data, each hit channel has the two-dimensional position, timing, and number of photoelectrons. The reconstruction of cosmic muon tracks are done by the P0D reconstruction software described in chapter 5. Event hits are separated into groups using the TFB timeslices. Each timeslice has an integration width of 250 ns with 70 ns dead time between two consecutive integration periods. Group which has more than 20 hits are searched for muon tracks. It is expected that there are around 28 hits from normal incident muons. Each reconstructed event has one 3D muon track. Events triggered by nearly vertical muons has no output track since the nearly vertical track fails the track matching using 2D tracks. Each 3D track has 3D

position, direction, timing and energy deposit at each tracking plane. Since the ECAL sections are thin, tracks in these sections are re-fitted to a single straight line. Figure shows the distribution of the cosine of the angle between the muon track and the z axis. Only tracks with $\cos\theta > 0.8$ are selected for light yield study. Fig. 6.7 shows the residuals of reconstructed 3D tracks. The residuals are defined as the difference between the charge-weighted position and the fitted track point position at each tracking plane. The residual distributions for xz and yz planes are defined separately. These residual distributions are fitted to a Gaussian function, the fitted parameters are $\mu_{x,y} = 0.0$ mm and $\sigma_x = 2.8$ mm, $\sigma_y = 3.2$ mm. These standard deviations are slightly larger than those from MC, $\sigma_{x,y} = 1.8$ mm. This could be because of the mis-alignment of scintillator bars in the actual detector.

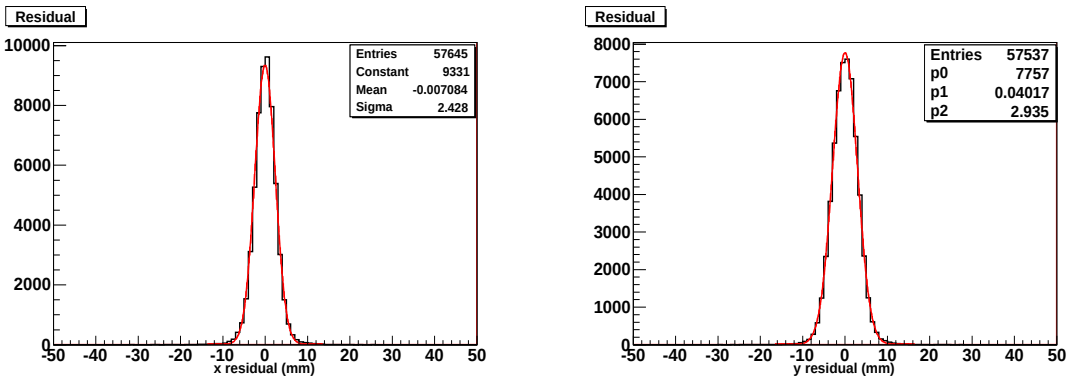

Figure 6.7: Residual distributions of reconstructed 3D tracks (solid histogram) in the xz (left) and yz (right) planes. The distributions are fitted to a Gaussian distribution (solid curve).

The triangular configuration is convenient since the point where a muon passes through a plane can be estimated from the two hit positions and their light yields

$$\bar{x} = \frac{Q_1 x_1 + Q_2 x_2}{Q_1 + Q_2} \tag{6.8}$$

$$= x_1 + p\gamma, \tag{6.9}$$

where p is the pitch (1.7 cm) and γ is the fractional light yield of the second bar:

$$\gamma = \frac{Q_2}{Q_1 + Q_2}. \tag{6.10}$$

The distribution of γ is shown in Fig. 6.8. Fig. 6.9 shows the hit map for one

tracking plane. One can clearly see the boundaries where the cosmic trigger primitive is not as efficient.

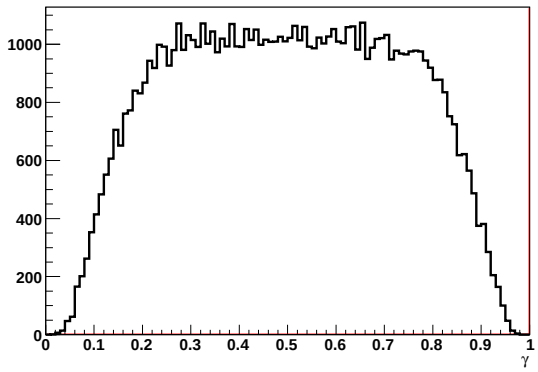

Figure 6.8: Fraction of light yield shared by two neighboring bars in the same plane.

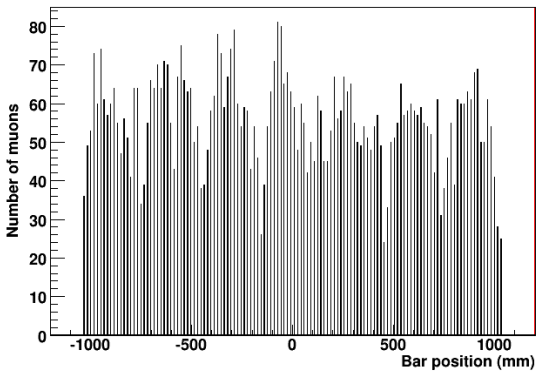

Figure 6.9: Hit map for one P0Dule (x layer).

Path length calculation Because of the triangular bar geometry, path length inside each bar must be calculated. This would not be necessary for the rectangular bar geometry where the path length is simply the bar thickness divided by the cosine of the incident angle. The path length is calculated using the geometry manager. The geometry manager holds all the information regarding the detector geometry. Specifically, the geometry manager can tell what bar volume a point belongs to. The fitted 3D track is parameterized by

a point line equation

$$\begin{aligned} x &= x_0 + l * t \\ y &= y_0 + m * t \\ z &= z_0 + n * t, \end{aligned} \tag{6.11}$$

where $M_0(x_0, y_0, z_0)$ is a point on the track and $\vec{s}_0(l, m, n)$ is the directional vector. The path length inside a bar is calculated by sampling points along the track with a step length Δt of 0.1 mm. Points are checked with the geometry manager to make sure that they are inside the bar. The path length is the product of the number of accepted points and the step length Δt. Assuming the position M_0 and direction $\vec{s}_0$ are accurate, this simple procedure only introduces a negligible uncertainty of 0.1 mm.

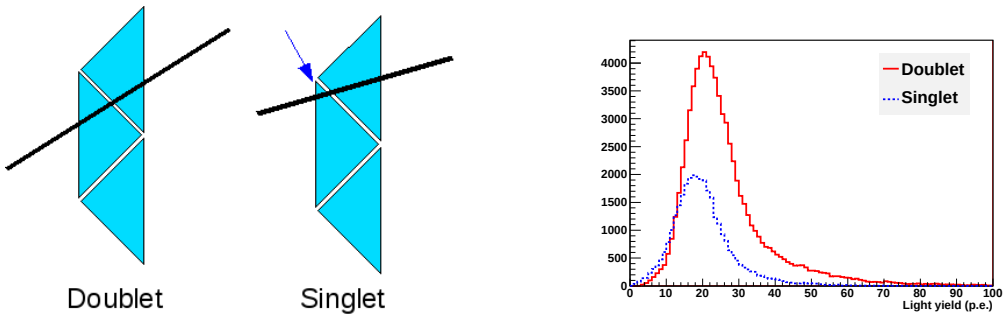

Figure 6.10: Illustration of singlet and doublet, central hole for WLS fiber is not shown (left), the black solid line represents a muon passing through, the arrow on the singlet shows where the muon clips the bar. Mean light yield per cm by MIP for singlets and doublets (right).

6.5 MIP light yield

6.5.1 Light yield

An important characteristic of minimum ionizing particles (MIP) is that their energy loss is weakly dependent on their energy, at high energy ($\sim$ 100 GeV) the energy loss rises only a few percent due to relativistic effects. Therefore, it is an good approximation to assume that the mean energy deposit per unit length by different MIP particles are the same. The number of photons produced by passing MIP particles in scintillator is proportional to the path length inside the scintillator volume. In order to compare the light yield from

tracks with different incident angles and positions, the light yield per unit path length is used. There are two ways to calculate the light yield per unit path length: from the light yield on each scintillator plane and from the light yield on each bar.

The light yield per unit path length can be calculated from that on each scintillator plane as follows. Most of the selected muons pass through two adjacent bars in the same scintillator plane. The path length in the two bars could be either comparable or very different, depending on the track position and direction. When the path lengths are comparable, there are two hits in the two bars, this is called a doublet. However, when one of the path lengths is small (a few millimeters), there could be no hit, or hit with light output less than the 2.5 p.e. threshold in one bar and hence there is only one hit from the other bar, this is called singlet. The doublet and singlet definition is illustrated in Fig. 6.10 (left). To study the variation of the light yield versus gain, only the yield calculated using doublets are used. In this case, the light yield per unit path length is simply the sum from the two bars of the doublets, corrected for the muon track direction and divided by scintillator plane thickness. The light yield per cm by MIP particles for both doublets and singlets is shown in Fig. 6.10. As expected, the mean of the singlets is slightly less than that of the doublets since there is contribution from only one bar. The mean light yield of the doublets is more than 20 p.e. per cm.

The light yield per unit path length can also be calculated by dividing the light yield in a bar by the path length in the same bar. The light yield obtained this way will be used to study the response of individual bars.

6.5.2 Correction for gain variation

Since the MPPC gain is sensitive to temperature change, its variation causes large fluctuations in the gain. The gain measurement has been described in. Fig. 6.11 (left) shows the mean gain over all the detector channels versus run number . The gain varies over the range from 9 ADC to 13 ADC. Fig. 6.11 (right) shows the mean light yield over all detector channels versus run number. It can be seen that the light yield follows the gain variation pattern. Fig. 6.12 shows the mean light yield versus gain for runs with $\Delta T < 0.2^0$C (triangle) and $\Delta T > 0.2^0$C (circle) separately. The plot shows an approximately linear relationship between the mean light yield and the gain for runs with $\Delta T < 0.2^0$C. The mean light yield from runs with $\Delta T > 0.2^0$C are mostly outliers since the greater the temperature change during a cosmic run, the less relevant the pedestal run. Remember that the calibration using pedestal run works properly only if the pedestal run and cosmic run have sim-

ilar running conditions. Therefore, the runs with $\Delta T > 0.2^0$C are excluded from the following study.

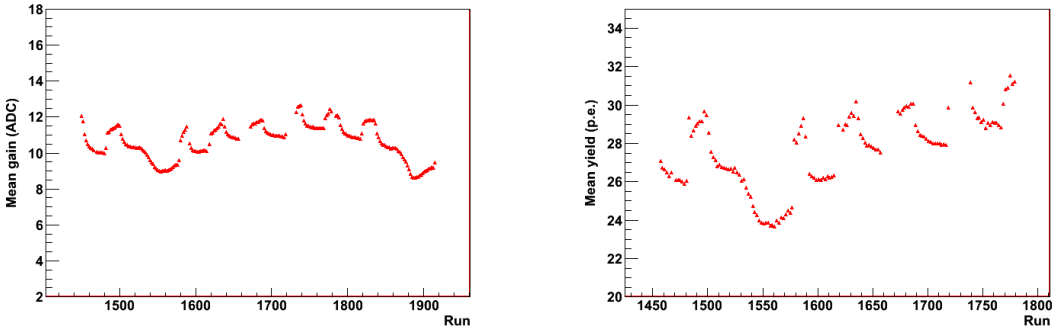

Figure 6.11: Mean gain over all the channels versus run number (left) and the mean yield versus run number (right).

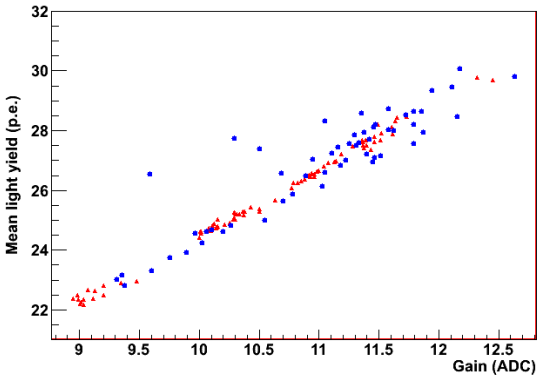

Figure 6.12: Mean light yield versus gain for runs with $\Delta T < 0.2^0$C (triangle) and $\Delta T > 0.2^0$C (circle).

Since the mean light yield varies greatly from run to run, in order to combine runs to increase muon statistics in scintillator bars requires correction for the gain variation. From Fig. 6.12, it is reasonable to assume that the mean light yield is a linear function of the gain,

$$Y = kG, \tag{6.12}$$

where Y is the mean light yield, G is the gain, and k is a proportional constant. It is assumed that the light yield vanishes at zero gain. Although this

assumption sounds intuitively reasonable, it might not be true if there is some small nonlinear effect. For now assuming that (6.12) is correct, the light yield Y at an arbitrary gain G can be related to that at some reference gain G_0:

$$Y_0 = \frac{Y}{1 + \frac{\Delta G}{G_0}}, \tag{6.13}$$

where $\Delta G = G - G_0$ is the gain deviation from the reference. The equation (6.13) says that Y_0 can be obtained from Y given the gain change ΔG. The correction factor is:

$$\frac{1}{1 + \frac{\Delta G}{G_0}} \tag{6.14}$$

It is remarkable that the correction factor does not depend on the proportional constant k. This means that the light yield can be corrected even before the muon track reconstruction and the light yield calculation. In this case the gain variation correction can be applied at the same time as the one photoelectron calibration. Fig. 6.13 shows the corrected light yield versus run number.

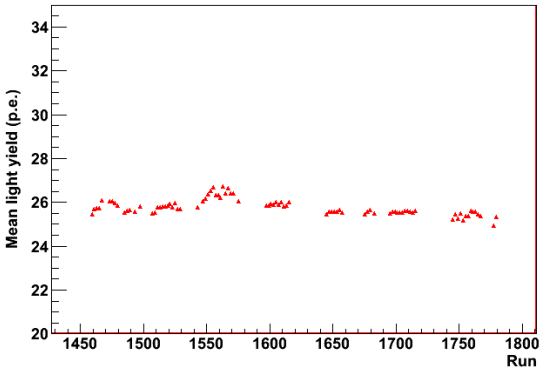

Figure 6.13: Corrected light yield using (6.14) versus run number.

We have seen that the simple model (6.12) can reduce the light yield variation over runs significantly, however, it is not adequate. Let us consider the case where the intercept is not zero,

$$Y = kG + b. \tag{6.15}$$

The correction factor becomes:

$$\frac{1}{1 + \alpha\frac{\Delta G}{G_0}} \text{ where } \alpha = \frac{1}{(1 + \frac{b}{kG_0})} \tag{6.16}$$

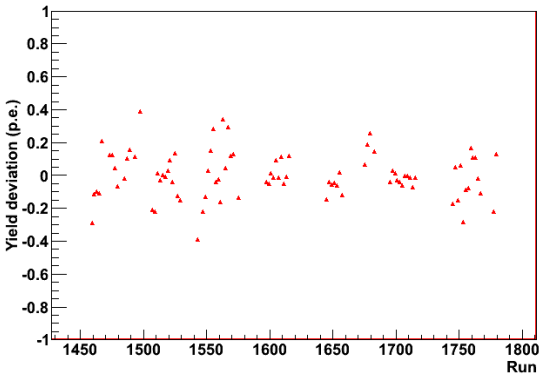

Figure 6.14: Corrected light yield using (6.17) versus run number.

The nonzero intercept adds a second term to the coefficient of $\Delta G/G_0$ which effectively reduces the correction. The parameters (k, b) appearing in the correction factor can be obtained from the cosmic data by fitting the plot in Fig. 6.12 ($\Delta T < 0.2$) to (6.15). Substituting the fitted parameters into (6.17), we obtain the empirical correction factor

$$\frac{1}{1 + 0.85\frac{\Delta G}{G_0}}. \tag{6.17}$$

After applying this correction factor, the light yield variation from run to run is further reduced, around ± 0.2 p.e. as shown in Fig. 6.14.

6.6 Light attenuation measurement

Light attenuation along WLS fiber can be measured using cosmic ray muons. This is done by comparing the mean light yield from different segments along the fiber. The mean shifts to a lower value for segments further away from the sensor.

After correction for the gain change due to temperature variation during the data taking period, muons from different runs can be combined to increase the statistics for light attenuation measurement. The number of muons per bar after combination is about from 10,000 to 15,000. To calculate the light attenuation curve, each bar is divided into segments, each of 20 cm length. The mean light yield of the muons in each segment is calculated. Since each bar has different response, the means from these segments are normalized by the mean from the segment in the middle of the fiber. After normalization, the means from the same segment of all the bars are combined. Fig. shows the mean distributions from two segments, one at -60cm and the other at +60cm. It is remembered that the sensor is at the positive side. It can be seen from the plot that the mean shifts to a lower value for segment further away from the sensor. This is resulted from light attenuation along the fibers. The means from all the segments versus the segment position are shown in Fig. 6.15. It can be seen that thanks to the mirror, there is much less light attenuation compared with that in case without the mirror. These points are fitted to a double exponential function $a(z)$ which parameterizes the attenuation:

$$a(z) = c_0 e^{-\frac{z}{l}} + c_0 r e^{\frac{z-2L}{l}} + c_1 e^{\frac{-z}{s}}, \tag{6.18}$$

where

- z is the distance from the light source to the sensor
- c_0, c_1 are amplitudes of the long and short components
- l, s are the long, and short attenuation lengths
- r is the mirror reflectivity
- L is the length of the bar

The fitted curve is shown (solid line) in the same plot.

The fitted attenuation curve is used to correct for the effect of light attenuation. To demonstrate the effectiveness of this curve, in Fig. we show the profile of the mean light yield versus position along fiber for one bar. It can be seen that the mean light yield is flat to within $\pm 1 p.e.$ along the bar.

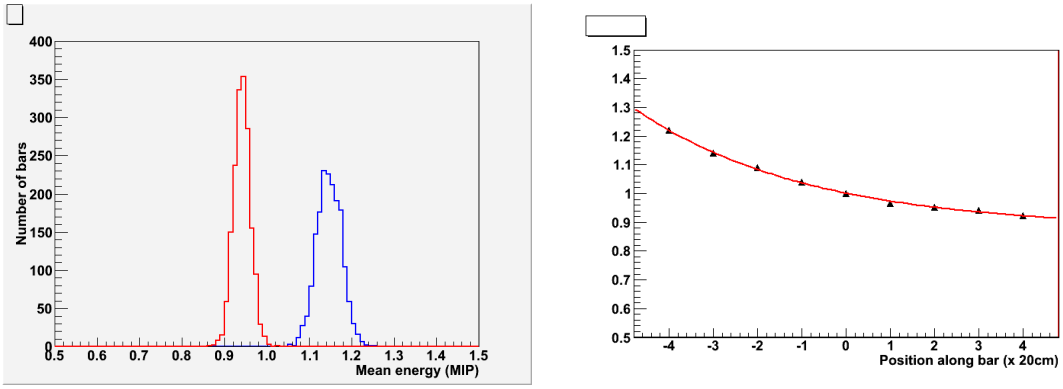

Figure 6.15: Energy distribution from segments at ±60 cm, mean shifts to lower value for the segment further away from the sensor (left). Light attenuation along WLS fiber. Solid (red) line is the fitted double exponential function (right).

6.7 Energy calibration using cosmic muons

6.7.1 Scintillator bar light yield

It was mentioned in Sect. 5 that the light yield per unit length of each bar is simply the light yield divided by the corresponding path length. How to calculate the path length is described in Sect. 4. The light yield after correction for light attenuation and path length for one channel is shown in Fig. 6.17 (left). The peak of the light yield distribution can be determined by fitting it to a Gaussian-convoluted Landau distribution. Fig. 6.17 (right) shows the distribution of peak light yield all the channels in the upstream ECAL. The distributions for X (solid) and Y (dashed) bars are shown separately. The number channels are fewer than the total number of channels in the detector since some bars, especially those at the corner or bottom of the detector, do not have many passing muons.

6.7.2 Energy calibration

The light attenuation in fibers has been measured using cosmic data and parameterized by the attenuation curve. This curve is used to correct for light attenuation before the energy calibration. The following corrections are applied on the light yield of every track hit:

- Path length: Given the track position and direction, the path length in any hit bar can be calculated as described above. The path length

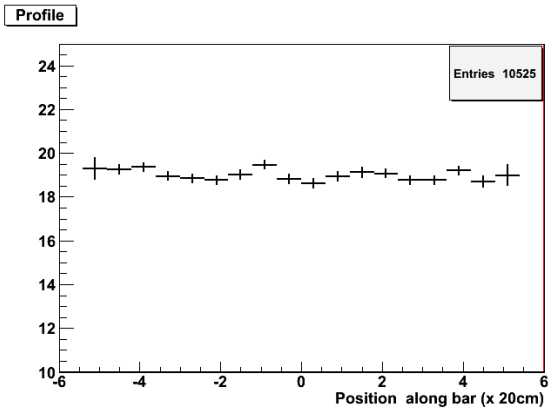

Figure 6.16: Mean light yield along the fiber after light attenuation correction for one bar.

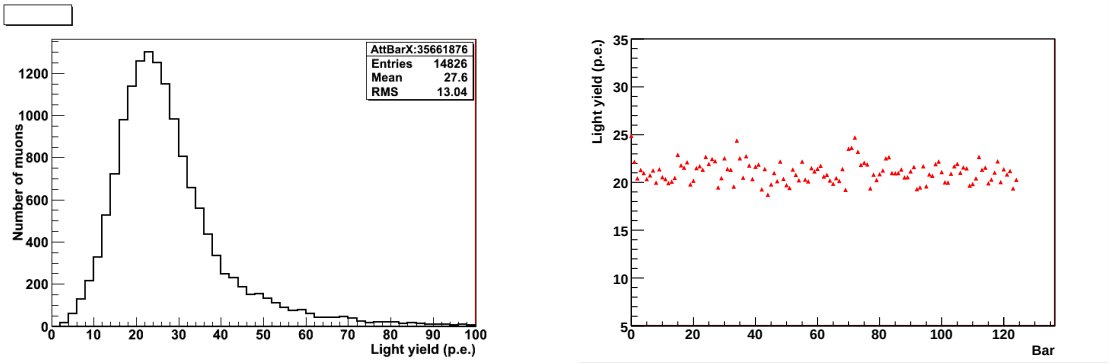

Figure 6.17: Light yield per cm after light attenuation correction of one channel (left). Mean light yield of all (X) channels on one P0Dule (right).

automatically includes the correction for track direction.

- Light attenuation are corrected using the attenuation curve given the distance from the hit to the sensor. This distance is available for hits associated with 3D tracks.

After these corrections, the light output difference from channel to channel is caused by the difference in channel response. These include the non-uniformity of scintillator bars, fibers, mirrors, fiber-sensor couplings, etc. In other words, these include all the time-independent difference from channel to channel. For each channel, the calibrated energy deposit by a muon in the unit of one MIP per cm is given by

$$E(\text{MIP}) = \frac{Y}{Y_0}, \tag{6.19}$$

where Y_0 is the mean light yield of the channel. The mean light yield of each channel is used as a calibration constant to account for the channel-to-channel response difference. These calibration constants are tested using a different set of cosmic runs. Remember that there is only temperature data for runs up to 1779, which are used to generate the calibration constants. Runs beyond this range can be used to test the calibration constants. Without temperature data, it is not possible to know if the gain correction is effective and hence only a subset of consecutive runs with similar gain are selected for testing. After the correction for gain variation, the path length and attenuation corrections are applied, and then the calibrated energy is calculated using (6.19). Fig. 6.18 shows the mean calibrated energy of all the (X) bars on one P0Dule. It can be seen that the mean energies from all the bars are uniform. The plot on the right shows the distribution of the calibrated mean energy of all the bars in the upsteam ECAL, the standard deviation of the distribution is ~ 0.01.

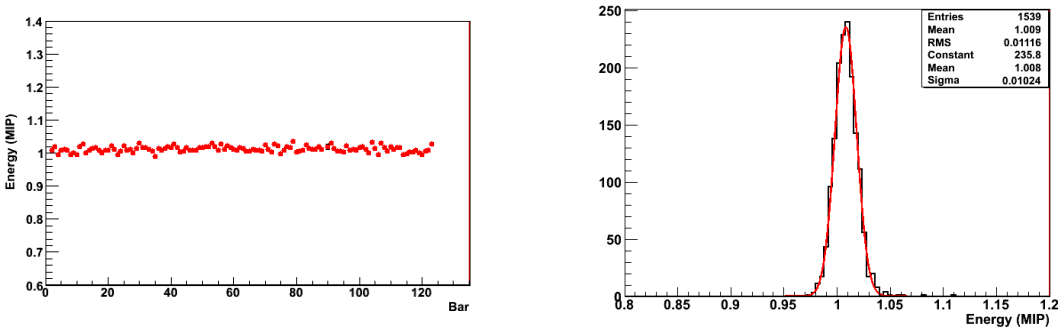

Figure 6.18: Mean calibrated energy of all (X) bars on one P0Dule and the distribution of calibrated energy of all the bars in the upstream ECAL.

CONCLUSION

The T2K experiment is a long baseline neutrino oscillation experiment that uses the intense ν_μ beam from J-PARC and Super-Kamiokande to make precision measurements of the atmospheric oscillation parameters, $(\Delta m^2_{32}, \sin^2 2\theta_{23})$ and search for ν_e appearance to improve by ten times the current limit the sensitivity on the last mixing angle, θ_{13}. One of the dominant backgrounds to the ν_e search is the single π^0 from ν_μ neutral current interactions. This background will be measured at the near site by the P0D and then extrapolated to the Super-Kamiokande. The P0D is built by a group of US institutions led by Stony Brook.

In this thesis, we have developed the event reconstruction and the energy calibration procedure using cosmic muons for the P0D. The event reconstruction has been tested using the MC simulated data. The rejection efficiency for charged current interactions is greater than 99%. The reconstruction efficiency for single π^0 from neutral current interactions is 18% and the purity of the final π^0 sample is 44.5%. For the energy calibration using cosmic muons, we have developed the procedure to correct for gain change. The light yield after correction is uniform within ± 0.2 p.e or 1%. We have also measured the light attenuation curve for WLS fibers. Finally, by using the light yield measurement with cosmic muons, we have been able to correct for channel response difference. The calibrated energies from all the channels in the upstream ECAL is uniform and the standard deviation of the calibrated energy distribution is ~ 0.01.

The T2K experiment started!

The event display shows the first cosmic muon passing all the sub-detectors in the basket. The near detector is ready for neutrino beam.

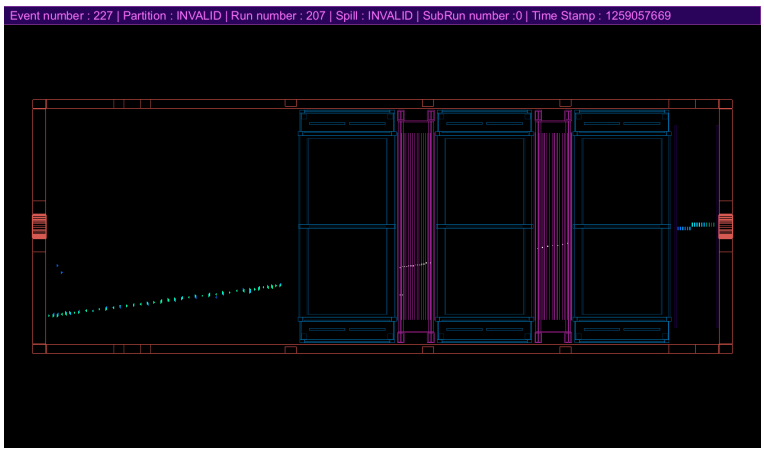

Figure 6.19: First cosmic muon event crossing all sub-detectors in the basket.

Bibliography

[1] The LEP Collaborations and the LEP Electroweak Working Group, as reported by J. Dress at the XX International Symposium on Lepton and Photon Interactions at High Energy, Rome, Italy (2001).

[2] A. I. Belesev *et al.* , Phys. Lett. B 350 263 (1995)

[3] V. Lobashev, in Proc. of 27th Int. Conf. on HEP (Glasgow, Scotland,1994)

[4] Ch. Weinheimer *et al.* , Physics Letters B 460 219 (1999)

[5] Katrin collaboration, Letter of Intent (2001), hep-ex/0109033

[6] B.H.J. McKellar Phys. Lett. B 97 93 (1980)

[7] K. Assamagan *et al.* , Phys. Lett. B 335 231 (1994)

[8] S. M. Bilenky, S.T. Petcov, Rev. Mod. Phys. 59 671 (1987)

[9] B. Pontecorvo, Sov.Phys.JETP 6 429 (1957)

[10] M. Bilenky, J. Hosek, S.T. Petcov, Phys.Lett. B94, 495 (1980); M. Doi *et al.*, Phys.Lett.B102 323 (1981).

[11] Langacker *et al.*, Nucl. Phys. B 282, 589 (1987)

[12] L. L. Chau, W. Y. Keung, Phys.Rev.Lett.53:1802 (1984)

[13] Z. Maki, M. Nakagawa, S. Sakata, Prog.Theor.Phys.28:870 (1962)

[14] S.P.Mikheyev and A. Yu. Smirnov, Yad. Fiz. 42, 1441(1985); L.Wolfenstein, Phys. Rev. D 17, 2369 (1978).

[15] H.W. Zaglauer and K.H. Schwarzer, Z. Phys. C 40, 273 (1988); V. Barger,K. Whisnant, S. Pakvasa and R. J. N. Phillips, Phys.Rev.D22, 2718 (1980).

[16] M. Freund, Phys. Rev. D 64, 053003 (2001); M. Freund, M. Linder, S.T. Petcov and A. Romanino, Nucl. Phys. B578, 27 (2000); A. Cervera *et al.*, Nucl. Phys. (Proc. Suppl.) B579, 17 (2000)

[17] Y. Fukuda et al., Phys.Rev.Lett.81 1562 (1998)

[18] Fukuda S, et al., Phys. Lett. B 539 179 (2002)

[19] Q.R. Ahmad *et al.*, Phys.Rev.Lett.89, 011301 (2002)

[20] Ahn MH, *et al.*, Phys. Rev. D 74 072003 (2006)

[21] MINOS Collaboration, Fermilab Report No. NuMI-L-375 (1998)

[22] S. Abe, *et al.*, Phys. Rev. Lett. 100, 221803 (2008)

[23] M. Apollonio *et al.*, Phys. Lett. B 466, 415 (1999)

[24] J. N. Bahcall, M.H. Pinsonneault, Rev.Mod.Phys.67 781 (1995); Rev.Mod.Phys.64 885 (1992); J. N. Bahcall, M.H. Pinsonneault, Sarbani Basu, Astrophys.J.555 990 (2001).

[25] J.N. Abdurashitov,*et al.* Phys. Rev. C 60 055801 (1999)

[26] W. Hampel, *et al.* Phys. Lett. B 447:127 (1999)

[27] M. Altmann, et al. Phys. Lett. B 490 16 (2000)

[28] N. Hata, P. Langacker Phys. Rev. D 52:420 (1995)

[29] K. Heeger, R.G. Robertson Phys. Rev. Lett. 77:3720 (1996)

[30] Y. Ashie, *et al.* Phys. Rev. Lett. 93 101801 (2004)

[31] Y. Ashie, *et al.* Phys. Rev. D71 112005 (2005)

[32] MINOS collaboration, Phys. Rev. Lett. 101, 131802 (2008)

[33] F. Boehm *et al.* Phys. Rev. D 62 072002 (2000)

[34] F. Boehm*et al.* Phys. Rev. D 64 112001 (2001)

[35] M. Apollonio *et al.*, Eur. Phys. J. C27 331 (2003)

[36] E. Eguchi, *et al.* Phys. Rev. Lett. 90 021802 (2003)

[37] T2K Collaboration, Letter of Intent, hep-ex/0106019

[38] T2K ND280 Conceptual Design Report, T2K Internal Document (2005).

[39] D. Beavis, A. Carroll, I. Chiang, *et al.*, Proposal of BNL AGS E-889 (1995)

[40] E. Aliu, *et al.*, Phys. Rev. Lett. 94, 081802 (2005)

[41] Y. Fukuda, *et al.*, Nucl. Instrum. Meth. A 501, 418-462, (2003)

[42] K. Yamamoto *et al.*, IEEE Nuclear Science Symposium, 1094 (2006)

[43] F.Retiere *et al.* , Nucl. Instr. Meth. A 610 378 (2009)

[44] A. Vacheret, S. Greenwood, M. Noy, M. Raymond, and A. Weber, Nuclear Science Symposium Conference Record, 1984-1991 (2007)

[45] Y. Hayato, Nuclear Physics B 112 171 (2002)

[46] T.Yang, C.Andreopoulos, H.Gallagher, K.Hoffman and P.Kehayias, hep-ph/0904.4043

[47] GEANT4 collaboration, Nucl. Inst. Meth. A 506 (2003) 250-303, and IEEE Trans. on Nucl. Sci. 53 No. 1 270 (2006)

[48] P.V.C. Hough, Machine Analysis of Bubble Chamber Pictures, Proc. Int. Conf. High Energy Accelerators and Instrumentation (1959)

[49] Sander J., Ester M., Kriegel H.-P., Xu X, Data Mining and Knowledge Discovery, Vol. 2, p.169 (1998).

[50] R.E. Kalman, Transaction of the ASME, Journal of Basic Engineering, 35-45 (1960).